การจำลองเชิงตัวเลขของคลื่นสึนามิในมหาสมุทรอินเดียเมื่อวันที่ 26 ธันวาคม 2547

นายณรงค์ฤทธิ์ แก้วบรรจักร์

วิทยานิพนธ์นี้เป็นส่วนหนึ่งของการศึกษาตามหลักสูตรปริญญาวิทยาศาสตรมหาบัณฑิต
สาขาวิชาวิทยาการคณนา ภาควิชาคณิตศาสตร์
คณะวิทยาศาสตร์ จุฬาลงกรณ์มหาวิทยาลัย
ปีการศึกษา 2548

ISBN 974-17-5291-1

NUMERICAL SIMULATION OF THE DECEMBER 26, 2004 :INDIAN OCEAN TSUNAMI

Mr. Narongrit Kaewbangak

A Thesis Submitted in Partial Fulfillment of the Requirements
for the Degree of Master of Science Program in Computational Science

Department of Mathematics
Faculty of Science
Chulalongkorn University

Academic year 2005
ISBN 974-17-5291-1

Thesis Title	NUMERICAL SIMULATION OF THE DECEMBER 26, 2004 :INDIAN OCEAN TSUNAMI
By	Mr. Narongrit Kaewbangak
Field of study	Computational Science
Thesis Advisor	Associate Professor Jack Asavanant, Ph.D.
Thesis Co-advisor	Mansour Ioualalen, Ph.D.

Accepted by the Faculty of Science, Chulalongkorn University in Partial Fulfillment of the Requirements for the Master's Degree

..... Dean of the Faculty of Science

(Professor Piamsak Menasveta,Ph.D.)

THESIS COMMITTEE

..... Chairman

(Associate Professor Suchada Siripant)

..... Thesis Advisor

(Associate Professor Jack Asavanant, Ph.D.)

..... Thesis Co-advisor

(Mansour Ioualalen, Ph.D.)

..... Member

(Assistant Professor Vimolrat Ngamaramvaranggul, Ph.D.)

ณรงค์ฤทธิ์ แก้วบรรจักร์ : การจำลองเชิงตัวเลขของคลื่นสึนามิในมหาสมุทรอินเดียเมื่อวันที่ 26 ธันวาคม 2547 (NUMERICAL SIMULATION OF THE DECEMBER 26, 2004: INDIAN OCEAN TSUNAMI) อ. ที่ปรึกษา : รองศาสตราจารย์ ดร.จักษ์ อัศวานันท์, อ.ที่ปรึกษาร่วม : Dr. MANSOUR IOUALALEN 80 หน้า. ISBN 974-17-5291-1.

เมื่อวันที่ 26 ธันวาคม 2547 เวลา 0:58:53 (GTM) ได้เกิดแผ่นดินไหวครั้งใหญ่ด้านชายฝั่งตะวันตกทางตอนเหนือของเกาะสุมาตรา ประเทศอินโดนีเซีย มีความรุนแรงขนาด 9.1-9.3 ริคเตอร์ จนเป็นสาเหตุที่ทำให้เกิดคลื่นสึนามิในมหาสมุทรอินเดีย

ในการศึกษานี้ เราใช้ลักษณะของแหล่งกำเนิดแผ่นดินไหวที่เหมาะสมที่สุดสำหรับการเกิดคลื่นสึนามิซึ่งอยู่บนพื้นฐานของข้อมูลทางธรณีฟิสิกส์และข้อมูลการสั่นสะเทือน และทำการจำลองเชิงตัวเลขโดยใช้แบบจำลอง GEOWAVE ซึ่งประกอบด้วย 2 ส่วน คือ ส่วนของการเกิดแผ่นดินไหวและส่วนของการแผ่ตัวของคลื่น การจำลองเชิงตัวเลขในส่วนของแผ่นดินไหวใช้วิธีการของ Okada (1985) และผลที่ได้จะนำไปใช้เป็นค่าเริ่มต้นของการคำนวณการแผ่ตัวของคลื่นที่สอดคล้องกับสมการ Fully Nonlinear Boussinesq อันดับสอง ในการตรวจสอบความถูกต้องของแหล่งกำเนิดสึนามิ เราใช้ข้อมูลระดับน้ำที่วัดได้ในช่วงเวลาที่เกิดคลื่นสึนามิจริง จากสถานีวัดระดับน้ำขึ้น-น้ำลงตามแนวชายฝั่งมหาสมุทรอินเดีย และข้อมูลที่ถูกบันทึกโดย Jason1 altimeter (track 129, cycle 109) นอกจากนั้นแล้ว เราได้เปรียบเทียบความสูงของคลื่นตามแนวชายฝั่งที่ได้จากการจำลองเชิงตัวเลขกับข้อมูลที่ได้จากการสังเกตตามแนวชายฝั่งทะเลอันดามัน ประเทศไทย เป็นกรณีศึกษาด้วย

ภาควิชา คณิตศาสตร์ ลายมือชื่อนิสิต.....
สาขาวิชา วิทยาการคณนา ลายมือชื่ออาจารย์ที่ปรึกษา.....
ปีการศึกษา 2548 ลายมือชื่ออาจารย์ที่ปรึกษาร่วม.....

4772286823 : MAJOR COMPUTATIONAL SCIENCE

KEY WORD: TSUNAMI SIMULATION / BOUSSINESQ WAVE MODEL/ NONLINEAR SHALLOW WATER WAVE MODEL / TSUNAMI SOURCE / WAVE PROPAGATION / MAXIMUM WAVE HEIGHT

NARONGRIT KAEWBANGAK : NUMERICAL SIMULATION OF THE DECEMBER 26, 2004: INDIAN OCEAN TSUNAMI. THESIS ADVISOR : ASSOC. PROF. JACK ASAVANANT, Ph.D., THESIS CO-ADVISOR : MANSOUR IOUALALEN, Ph.D., 80 pp. ISBN 974-17-5291-1.

The December 26, 2004 tsunami is one of the most devastating tsunami in recorded history. It was generated in the Indian Ocean off the western coast of northern Sumatra, Indonesia at 0:58:53 (GMT) by one of the largest earthquake of the century with a earthquake magnitude of M_w=9.1-9.3.

In this study, we focus on the best-fitted tsunami source based on geophysical and seismological data, and the use of accurate bathymetry and topography data. Then, we simulated the large scale features of the tsunami propagation, runup and inundation. The numerical simulation is performed using GEOWAVE model. GEOWAVE consists of two components: the modeling of the tsunami source (Okada, 1985), and the computation of the wave propagation and inundation based on a second-order fully nonlinear Boussinesq equations. The tsunami source is used as initial condition in the tsunami propagation and inundation model. The tsunami source model is calibrated by using available tide gauge data and anomalous water elevations recorded by Jason1 altimeter (track 129, cycle 109). The simulated maximum wave heights for the Indian Ocean are displayed and compared with observations with a special focus on the Thailand coast.

Department **Mathematics** Student's signature Narongrit Kaewbangak

Field of study **Computational Science** Advisor's signature Jack Asavanant

Academic year **2005** Co-advisor's signature Mansour Ioualalen

ACKNOWLEDGEMENTS

I am greatful to my supervisor, Associate Professor Dr. Jack Asavanant, to whom with his advice, guidance and care for helping me to overcome the neccessary difficulties in the course of this study and make this dissertation possible. I would also like to thank my co-supervisor, Dr.Mansour Ioualalen at Geosciences Azur (IRD, CNRS, UPMC, UNSA), Villefranche-sur-Mer, France, who provided me a wonderful suggestions in research methodologies.

I would like to gratefully acknowledge the National Electronics and Computer Technology Center (NECTEC) under the Ministry of Science and Technology, Thailand for the used of their ITANIUM computer cluster, Dr. Pramot Sojisuporn from Marine Science Department, Chulalongkorn University for providing water level data and Dr. Anond Snidvongs, Head of Chulalongkorn University Tsunami Rehabilitation Research Center, for providing the digitized inland topography and sea bottom bathymetry along the westcoast of Thailand.

Also, I would like to thank the chairman and member of the committee of this the thesis, Associate Professor Suchada Siripant and Assistant Professor Dr. Vimolrat Ngamaramvaranggul, who made helpful comments on the suitability of thesis content. Besides, I feel very thankful to all of my teachers who have taught me advance knowledge and skill. In particular, I must also extend my thanks to Advanced Virtual and Intelligent Computing (AVIC) Center and Department of Mathematics for various forms of help in particular computer facilities.

Finally, I would like express my sincere gratitude to my beloved parents for their kind encouragement throughout my study.

TABLE OF CONTENTS

CHAPTER Page

LIST OF TABLES

LIST OF FIGURES

FIGURE Page

CHAPTER I

INTRODUCTION

The tsunami phenomenon is a series of waves of extremely long wavelength and period generated in a body of water by an impulsive disturbance that displaces the water. Tsunamis are sometimes called "seismic sea waves".

1.1 Tsunami Generality

Tsunamis are shallow-water waves, which mean that the ratio between water depth and wavelength is very small. In open sea, these shallow-water waves move at a speed equal to the square root of the product of the gravitational acceleration (9.8 m/s^2) and the water depth. For example, when the ocean is 5,000 m deep, a tsunami travels at about 800 km/hr. At this speed, the wave can compete with an airplane traveling around the world in less than 2 days. However, in deep water a tsunami is not dangerous since a single wave is less than a few meters high despite its high speed. For example, fishermen twenty miles out in the sea cannot realize the wave passing under their boats because it probably has a height at the time of about 0.5 m and its wavelength may be too long to be noticed.

When a tsunami moves into the shallow water of coastal zone, its speed and wavelength decrease whereas the amplitude increases. Tsunami can reach a maximum onshore vertical height (called a run up) of several meters. With such maximum wave height together with a destructive energy carried from its source to coastline, almost

everything can be swept clean.

A tsunami is a long internal gravity wave which signature at the surface can be important. The wavelength varies from a few to hundreds kilometers, while its period may vary from a few to several tens of minutes. These characteristics explain why 1) such a wave may propagate over an entire ocean basin without being significantly dissipated, 2) water particle velocity at the ocean bottom is locally quasi-uniform, generating important sediments and materials attachments, and 3) the wave is generally materialized at the coast by a rapid inundation instead of usual wave breaking. These characteristics differentiate a tsunami from an ordinary short-wave (swell) because, along the direction of propagation, water particles describe a flat ellipse and a circular trajectory respectively. As a result, the shear forces, yielding attachments, are much more important in the case of long wave tsunamis. Since the tsunami oscillates over the whole water column (even in deep ocean), this effect is enhanced compared to the swell whose wind mechanical force is exerted only near the surface. Because of such potential attachments, even a weak amplitude tsunami (tens of centimeters) may generate serious damages at the coast : rapid inundation, ocean bottom erosion by currents yielding waters that can be saturated by marine sediments, transported materials (marine or onshore), or simply, a weak resistance that one may have against the strong horizonatal currents.

Offshore, the wave speed of propagation is quasi-linear and is directly related to the ocean bathymetry. For 4000 m and 50 m water depths the tsunami propagates at 700 km/hr and 80 km/hr respectively. Consequently, the bathymetry map determines the tsunami time arrival at any point of the globe. This is a crucial information for a warning system protocol as far as the tsunami source has been localized.

Several processes amplify the tsunami wave height approach in the coast : 1) the wave energy is conserved and confined in a shrinking water volume, 2) wave crests accumulate (wave focusing) through diffraction and bathymetry gradient.

A tsunami is triggred when the water column is deformed over an extended horizontal direction generating a long internal wave. This is the case for a co-seismic displacement of the sea bottom immediatly after an earthquake, for large volume landslides (submarine or subaerial) or through rapid and large volcanic eruptions. It is often difficult to identify the respective tsunami contributions sources when several of them are tsunamigenic. This can be the case when an earthquake (tsunamigenic or not) has triggered a landslide. In such configurations, numerical simulations may help and it is always fruitful to perform bathymetric surveys of the area in order to locate eventual landslide scars and estimate its volume and mode of sliding. The usual procedure is to perform several numerical simulations for diffrent sources that describe at best the observations in order to extract their respective contributions.

1.2 The 2004 Indian Ocean Tsunami

On December 26, 2004 at 0:58:53 GMT a 9.1-9.3 Magnitude earthquake occurred along 1300 km of the Sundra and Andaman trenches in the eastern Indian Ocean, approximately 160 km off west coast of northern Sumatra. The main shock epicenter was located at 3.32° N and 95.85° E, 25-30 km deep. Over 200,000 people across the entire Indian Ocean basin were killed with tens of thousands reported missing as a result of this disastrous event. In accordance with modern practice, several international scientific team were organized to conduct quantitative survey of the tsunami characteristics and hazard analysis in the impacted coastal regions. Numerous detailed eyewitness observations were also reported in the form of video digital recordings.

In this tsunami event, there were several international scientific survey teams (e.g., International Tsunami Survey Team of Indian Ocean Tsunami Disaster) as well as a group of Thai scientists from Department of Mineral Resources (DMR), Ministry of

Natural Resources and Environments, Thailand) conducting the tsunami impact investigation on the coastal regions of Thailand. The damaged coastline extended over the six provinces of Thailand: Ranong, Phang Nga, Phuket, Krabi, Trang, and Satun. For these tsunami affected areas, Phang Nga province experienced the most fatalities, thousands of missing people, and widespread destructions especially at Khao Lak coastline where the highest runup was recorded. Most of the fisherman villages and their ecological environments were destroyed completely including the seriously damaged cultural landscapes in parts of Phang Nga and Krabi Provinces.

1.3 Objective and Scope of the Thesis

The goal of this thesis was to simulate the generation, the propagation and inundation of tsunami on the December 26, 2004 and to better understand this phenomenon especially in the Andaman sea coast of Thailand.

In this thesis, we focus on the best-fitted tsunami source based on geophysical and seismological data, and the use of accurate bathymetry and topography data. Then, we simulate the large scale features of tsunami propagation, runup and inundation. The numerical simulation is performed using GEOWAVE model. GEOWAVE consists of two components: the modeling of the tsunami source, and the computation of the wave propagation and inundation. The tsunami source is used as initial condition in the tsunami propagation and inundation model. The tsunami source calculation is based on the half-plane solution of an elastic dislocation problem (Okada, 1985). The propagation and inundation model for the numerical simulation is based on a second-order fully nonlinear Boussinesq equations. The tsunami source model is calibrated by using available tide gage data and anomalous water elevations recorded by the JASON 1 altimeter (track 129, cycle 109). The simulated maximum wave heights for the In-

dian Ocean are displayed and compared with observations with a special focus for the Thailand westcoast.

1.4 Outline of the Thesis

This thesis is organized as follows. Chapter II describes the geophysical and seismic characterization. Overview of the source, propagation and inundation models are given in Chapter III. Tsunami simulations are described in Chapter IV. In Chapter V, data and model calibrations are presented. Numerical results are discussed in Chapter VI. Concluding remarks are given in Chapter VII.

CHAPTER II

GEOPHYSICAL AND SEISMIC CHARACTERIZATION

2.1 Earthquake Generality

An earthquake is a trembling or shaking movement of the Earth's surface. Earthquakes typically result from the movement of faults, quasi-planar zones of deformation within its uppermost layers. The word earthquake is also widely used to indicate the source region itself. The solid earth is in slow but constant motion and earthquakes occur where the resulting stress exceeds the capacity of Earth materials to support it. This condition is most often found at (and the resulting frequent occurrence of earthquakes is used to define) the boundaries of the tectonic plates into which the Earth's lithosphere can be divided. Events that occur at plate boundaries are called interplate earthquakes; the less frequent events that occur in the interior of the lithospheric plates are called intraplate earthquakes.

2.1.1 Characteristics of Earthquake

Earthquakes occur every day on Earth, but the vast majorities of them are minor and cause no damage. Large earthquakes can cause serious destruction and massive loss of life via a variety of agents of damage including fault rupture, vibratory ground motion (i.e., shaking), inundation (e.g., tsunami, seiche , dam failure), various kinds of permanent ground failure (e.g. liquefaction, landslide), and fire or hazardous materials

release. In a particular earthquake, any of these agents of damage can dominate, and historically each has caused major damage and great loss of life, but for most of the earthquakes shaking is the dominant and most widespread cause of damage.

Most of the large earthquakes are accompanied by other, smaller ones, known as foreshocks when they occur before the principal or main shock and aftershocks when they occur following it. The source of an earthquake is distributed over a significant area , in the case of large earthquakes, over the entire planet. Ground motions caused by very distant earthquakes are called teleseisms. It is usually possible to identify a point from which the earthquake's seismic waves appear to emanate. That point is called its "focus"and usually proves to be the point at which fault rupture was initiated. The position of the focus is known as the "hypocenter"and the location on the surface directly above it is the "epicenter". Earthquakes, especially those that occur beneath sea or ocean-covered areas, can give rise to tsunamis, either as a direct result of the deformation of the sea bed due to the earthquake, or as a result of submarine landslips or "slides"indirectly triggered by it.

2.1.2 Causes of Earthquake

Some earthquakes are caused by the movement of magma in volcanoes, and such quakes can be an early warning of volcanic eruptions. A rare few earthquakes have been associated with the build-up of large masses of water behind dams, such as the Kariba Dam in Zambia, Africa, and with the injection or extraction of fluids into the Earth's crust (e.g., at certain geothermal power plants and at the Rocky Mountain Arsenal). Such earthquakes occur because the strength of the Earth's crust can be modified by fluid pressure. Finally, earthquakes (in a broad sense) can also result from the detonation of explosives. Thus scientists have been able to monitor, using the tools of seismology,

nuclear weapon tests performed by governments that were not disclosing information about these tests along normal channels. Earthquakes such as these that are caused by human activity are referred to by the term induced seismicity.

2.1.3 Tsunamis Generated by Earthquakes

Earthquakes create a disturbance of the seafloor causing tsunami. Thus, earthquakes that occur along coastlines or anywhere beneath the oceans can generate tsunami. The size of the tsunami is usually related to the size of the earthquake, with larger tsunami generated by larger earthquakes. The size of displacement is also important. Tsunamis are often generated when an earthquake causes vertical displacement of the seafloor. For example, in 1906, the earthquake occurred near San Francisco California had a Richter Magnitude of about 7.1, yet no tsunami was generated because the motion on the fault was strike-slip motion with no vertical displacement. Thus, tsunamis only occur if the fault generating the earthquake has normal or reverse displacement. Because of this, most tsunami are generated by earthquakes that occur along the subduction boundaries of plates, along the oceanic trenches.

2.2 The December 26, 2004 : Sumatra Earthquake

Large faults form over time, presumably, through small slip events followed in time by larger slip events (Wells *et al.*, 1994). Consequently, large single-event displacements tend to occur on structures that have already accumulated large total displacements. Therefore, the tectonic structures responsible for the December 26, 2004, event should be evident in the offshore bathymetry, unless they are buried under loose sediment. These structures are generally described as the Indo-Australian (or downgoing) plate subducting beneath the Eurasian (or overriding) plate at 50-60 mm per year, with a

largely East-West direction of convergence. The Bay of Bengal consists mostly of the Australian-Indian plate, with a sequence of islands running north-south along the eastern edge of the bay, denoting the plate boundaries and the edge of the subduction zone. In the Bay of Bengal, sediment from rivers contribute to a massive sediment fan that covers the entire downgoing plate from north to south, whose motion creates a large accretionary wedge east of the subduction zone. The subduction zone is thus visible along the entire rupture length, with deformation and erosion of the overriding plate in plain view.

The main shock of the December 26, 2004 earthquake occurred along the subduction zone between the downgoing Indo-Australian and overriding Eurasian plates, at a hypocentral depth of around 25-30 km from the surface (Ammon *et al.*, 2005). The main shock epicenter was located at 3.32° latitude N and 95.58° longitude E. The total rupture length is around 1,200-1,300 km requiring less than 10 min for the rupture to propagate end to end.

CHAPTER III

SOURCE, PROPAGATION AND INUNDATION MODELS

In this chapter, we give an overview and descriptions of the tsunami source, wave propagation and inundation models.

3.1 Source Model

The generation mechanism for the Indian Ocean tsunami is mainly due to the static sea floor uplift caused by abrupt slip at the Indian/Burma plate interface. Seismic inversion models (Ammon *et al.*, 2005) indicated that the main shock propagated northward from the epicenter parallel to the Sumatra trenches for approximately 1,200-1,300 km of the fault length.

The main generating force of a tsunami triggered by an earthquake is the uplift or subsidence of the sea-floor. Determining the actual extent of sea-floor change in a subsea earthquake is very difficult. In general, the displacement can be computed from the formula which output surface deformation as a function of fault strike, dip, slip, length, width, depth, moment magnitude, and Lame's constants for the surrounding rock (Okada, 1985). The underlying assumptions are based on the isotropic property and half-plane homogeneity of a simple source configuration. Our earthquake tsunami source is based on the standrad half-plane solution for an elastic dislocation with maximum slip Δ (Okada, 1985). Thus, we define an oblique planar fault of length L and width W, with centroid located at latitude-longitude (x_0, y_0) and depth d of earthquake at the centroid,

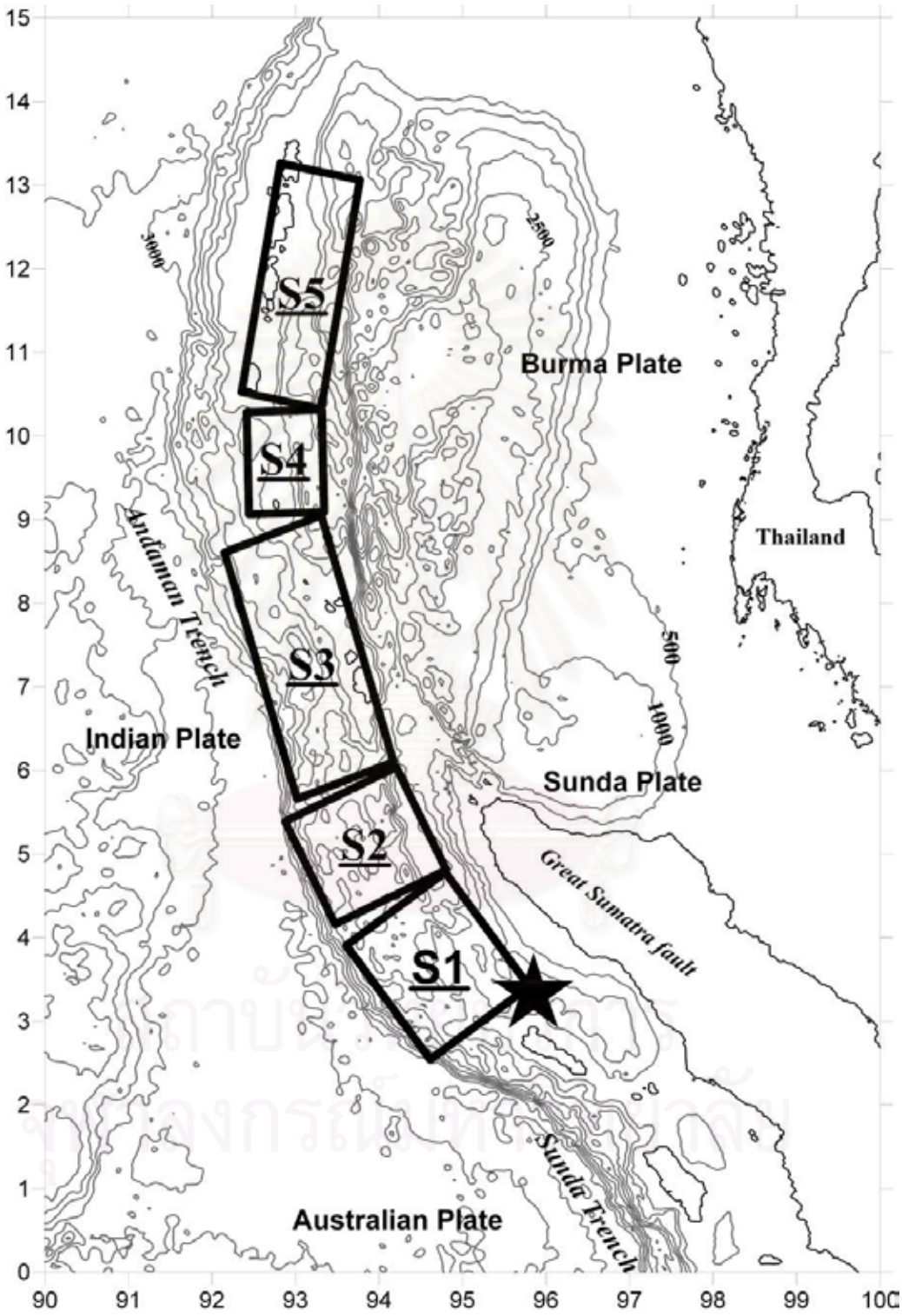

Figure 3.1: Earthquake Tsunami Source

and discretize it into many small trapezoids. The vertical co-seismic displacement on the ocean floor surrounding the fault is calculated by summing up contributions of point source elastic solutions, based on the actual depth of each trapezoid. The shear modulus μ can be specified as a function of depth and other seismic and geological descriptors, although it is assumed to be constant in this work. Okada's solution is implemented in TOPICS ("Tsunami Open and Progressive Initial Conditions System"), that provides the vertical co-seismic displacements as outputs, as well as a characteristic tsunami wavelength λ_0 (smaller of the fault dimensions L or W) and a characteristic tsunami period $T_0 \cong \lambda_0/\sqrt{gh}$. A characteristic initial tsunami amplitude η_0 can be defined as the minimum or maximum elevation found from coseismic displacement. The seismic moment M_0 is proportional to but slightly less than $\mu LW\Delta$ because a Gaussian slip distribution is assumed about the centroid. [The application of this methodology to landslide tsunami source is detialed in Watts *et al.* (2003)]

In this study, the ruptured subduction zone is identified by five segments of tsunami source based on different morphologies (Figure 3.1). Okada's formula computed ground displacement from fault parameters of each segment shown in Table 4.1.

3.2 Propagation and Inundation Models

Usually tsunamis are long waves (as compared with the ocean depth). Therefore, it is natural first to consider the long-wave (or shallow-water) approximation for the tsunami generation model. However, the shallow water equations ignore the frequency dispersion which can be important for the case of higher frequency wave propagation in relatively deep water.

Hence in this section, we will show an overview of the tsunami wave propagation and inundation models. In this study, we consider two principal models: nonlinear shallow

water wave and fully nonlinear Boussinesq wave models.

3.2.1 Fully Nonlinear Boussinesq Wave Model

Let us consider a three-dimensional wave field with water surface elevation $\eta(x, y, t)$ at arbitrary time t propagating over a variable water depth $h(x, y)$. A cartesian coordinate system (x, y, z) is adopted, with z measured upwards from the still-water level. The fluid is assumed to be inviscid and incompressible, and the flow is assumed to be irrotational. Following Wei *et al.* (1995), the fully nonlinear Boussinesq equations are given by:

$$\eta_t + \nabla \cdot \Big\{ (h+\eta) \Big[\mathbf{u}_\alpha + \Big(z_\alpha + \frac{1}{2}(h+\eta) \Big) \nabla(\nabla \cdot (h\mathbf{u}_\alpha)) + \Big(\frac{1}{2} z_\alpha^2 - \frac{1}{6} \Big(h^2 - h\eta + \eta^2 \Big) \Big) \nabla(\nabla \cdot \mathbf{u}_\alpha) \Big] \Big\} = 0 \tag{3.1}$$

$$\begin{aligned} &\mathbf{u}_{\alpha t} + (\mathbf{u}_\alpha \cdot \nabla)\mathbf{u}_\alpha + g\nabla\eta + z_\alpha \Big\{ \frac{1}{2} z_\alpha \nabla(\nabla \cdot \mathbf{u}_{\alpha t}) + \nabla(\nabla \cdot (h\mathbf{u}_{\alpha t})) \Big\} \\ &\quad + \nabla \Big\{ \frac{1}{2}(z_\alpha^2 - \eta^2)(\mathbf{u}_\alpha \cdot \nabla)(\nabla \cdot \mathbf{u}_\alpha) + \frac{1}{2}[\nabla \cdot (h\mathbf{u}_\alpha) + \eta \nabla \cdot \mathbf{u}_\alpha]^2 \Big\} \\ &\quad + \nabla \Big\{ (z_\alpha - \eta)(\mathbf{u}_\alpha \cdot \nabla)(\nabla \cdot (h\mathbf{u}_\alpha)) - \eta \Big[\frac{1}{2} \eta \nabla \cdot \mathbf{u}_{\alpha t} + \nabla \cdot (h\mathbf{u}_{\alpha t}) \Big] \Big\} = 0 \end{aligned} \tag{3.2}$$

where η is the surface elevation, h is the still water depth, $\mathbf{u}_\alpha$ is the horizotal velocity vector at the water depth $z = z_\alpha = -0.531h$, $\nabla = (\partial/\partial x, \partial/\partial y)$ is the horizontal gradient operator, g is the gravitational acceleration, and subscript t denotes the partial derivative with respect to time. Equations (3.1) and (3.2) signify the conservations of mass and momentum, respectively (see Appendix I for derivations).

3.2.2 Nonlinear Shallow Water Wave Model

For the nonlinear shallow water wave model, we replace velocity at a certain depth $\mathbf{u}_\alpha$ by the depth averaged velocity $\bar{\mathbf{u}}$ in the Boussinesq equations. Frequency dispersion

are also ignored. Hence the nonlinear shallow water wave model can be obtained after neglecting all dispersion term in (3.1) and (3.2), as follows

$$\eta_t + \nabla \cdot \left\{ (h+\eta)\bar{\mathbf{u}} \right\} = 0 \tag{3.3}$$

$$\bar{\mathbf{u}}_t + g\nabla\eta + (\bar{\mathbf{u}} \cdot \nabla)\bar{\mathbf{u}} = 0. \tag{3.4}$$

3.2.3 Modified Fully Nonlinear Boussinesq Wave Model

Equations (3.1) and (3.2) describe the frictionless evolution of nonbreaking waves over a smooth, impermeable bottom. In order to develop a model for practical application, sevaral effects have to be incorporated into the model scheme, including physical effects of frictional damping and wave breaking, as well as extentions needed to perform purely numerical tasks including wave generation, boundary absorbtion, and moving shoreline. We rewrite equations (3.1) and (3.2) by including these extensions as

$$\eta_t = E(\eta,u,v) + \gamma E_2(\eta,u,v) \tag{3.5}$$

$$\begin{aligned}[U(u)]_t =& F(\eta,u,v) + [F_1(v)]_t + \gamma[F_2(\eta,u,v) + F^t(\eta,u_t,v_t)] \\ &+ F_b + F_{br} + F_{bs} + F_{sp}\end{aligned} \tag{3.6}$$

$$\begin{aligned}[V(v)]_t =& G(\eta,u,v) + [G_1(u)]_t + \gamma[G_2(\eta,u,v) + G^t(\eta,u_t,v_t)] \\ &+ G_b + G_{br} + G_{bs} + G_{sp}\end{aligned} \tag{3.7}$$

Here u and v are the horizontal velocities in horizontal directions x and y at depth $z = z_\alpha = -0.531h$, i.e., $(u,v) = \mathbf{u}_\alpha$, and γ is a control parameter allowing us to choose between fully nonlinear ($\gamma = 1$) or weakly nonlinear ($\gamma = 0$) Boussinesq cases. The quantities $U, V, E, E_2, F, F_1, F_2, G, G_1, G_2, F^t$ and G^t are functions of η, u, v, u_t or v_t

which are defined as

$$U = u + h[b_1 h u_{xx} + b_2 (hu)_{xx}] \tag{3.8}$$

$$V = v + h[b_1 h v_{yy} + b_2 (hv)_{yy}] \tag{3.9}$$

$$\begin{aligned} E = & -\frac{1}{\kappa}[(\Lambda u)_x + (\Lambda v)_y] \\ & - \Big\{ a_1 h^3 (u_{xx} + v_{xy}) + a_2 h^2 [(hu)_{xx} + (hv)_{xy}] \Big\}_x \\ & - \Big\{ a_1 h^3 (u_{xy} + v_{yy}) + a_2 h^2 [(hu)_{xy} + (hv)_{yy}] \Big\}_y \end{aligned} \tag{3.10}$$

$$F = -g\eta_x - (uu_x + vu_y) \tag{3.11}$$

$$G = -g\eta_y - (uv_x + vv_y) \tag{3.12}$$

$$F_1 = -h[b_1 h v_{xy} + b_2 (hv)_{xy}] \tag{3.13}$$

$$G_1 = -h[b_1 h u_{xy} + b_2 (hu)_{xy}] \tag{3.14}$$

$$\begin{aligned} E_2 = & -\Big\{ \Big[a_1 h^2 \eta + \frac{1}{6}\eta(h^2 - \eta^2) \Big] (u_{xx} + v_{xy}) \Big\}_x \\ & - \Big\{ \Big[a_2 h\eta - \frac{1}{2}\eta(h + \eta) \Big] [(hu)_{xx} + (hv)_{xy}] \Big\}_x \\ & - \Big\{ \Big[a_1 h^2 \eta + \frac{1}{6}\eta(h^2 - \eta^2) \Big] (u_{xy} + v_{yy}) \Big\}_y \\ & - \Big\{ \Big[a_2 h\eta - \frac{1}{2}\eta(h + \eta) \Big] [(hu)_{xy} + (hv)_{yy}] \Big\}_y \end{aligned} \tag{3.15}$$

$$\begin{aligned} F_2 = & -\Big\{ \frac{1}{2}(z_\alpha^2 - \eta^2)[u(u_x + v_y)_x + v(u_x + v_y)_y] \Big\}_x \\ & - \Big\{ (z_\alpha - \eta)[u[(hu)_x + (hv)_y]_x + v[(hu)_x + (hv)_y]_y \Big\}_x \\ & - \frac{1}{2}\Big\{ [(hu)_x + (hv)_y + \eta(u_x + v_y)]^2 \Big\}_x \end{aligned} \tag{3.16}$$

$$\begin{aligned} G_2 = & -\Big\{ \frac{1}{2}(z_\alpha^2 - \eta^2)[u(u_x + v_y)_x + v(u_x + v_y)_y] \Big\}_y \\ & - \Big\{ (z_\alpha - \eta)[u[(hu)_x + (hv)_y]_x + v[(hu)_x + (hv)_y]_y \Big\}_y \\ & - \frac{1}{2}\Big\{ [(hu)_x + (hv)_y + \eta(u_x + v_y)]^2 \Big\}_y \end{aligned} \tag{3.17}$$

$$F^t = \left\{ \frac{1}{2}\eta^2[(u_t)_x + (v_t)_y] + \eta[[h(u_t)]_x + [h(v_t)]_y] \right\}_x \tag{3.18}$$

$$G^t = \left\{ \frac{1}{2}\eta^2[(u_t)_x + (v_t)_y] + \eta[[h(u_t)]_x + [h(v_t)]_y] \right\}_y \tag{3.19}$$

where a_1, a_2, b_1, b_2 are constants which are related to the dimensionless referenced water depth $\beta = z_\alpha/h = -0.531$ by

$$a_1 = \frac{1}{2}\beta^2 - \frac{1}{6}, \quad a_2 = \beta + \frac{1}{2}, \quad b_1 = \frac{1}{2}\beta^2, \quad b_2 = \beta \tag{3.20}$$

The factors Λ and κ in (3.10) are provided for a treatment of moving shorelines, which were introduce by Kennedy *et al.* (2000) and Chen *et al.* (2000). The remaining terms are added to the model for some specific tasks. First, the vector (F_b, G_b) in (3.6-3.7) is the bottom friction vector. Secondly, the vector (F_{br}, G_{br}) appearing in (3.6-3.7) is the wave breaking model. Finally, Smogorinsky-type subgrid model is introduced by (F_{bs}, G_{bs}) to account for the effects of unresolved turbulence on the computed flow field. These are shown in Appendix II.

The vector (F_{sp}, G_{sp}) represents the wave absorption term due to damping effects at the model boundaries (detailed in Appendix III).

CHAPTER IV

TSUNAMI SIMULATIONS

4.1 Construction of Model Grid

We construct the numerical simulation grid by using ETOPO2 bathymetry and topography data together with denser and more accurate digitized bathymetry and topography data along the Andaman sea coast of Thailand (Figure 4.1) provided by Chulalongkorn University Tsunami Rehabilitation Research Center. These data were derived by a composite approach using 30 m NASA's Space Shuttle Radar Topography Mission (SRTM) data for the land area with digitized navigational chart (Hydrographic Department of the Royal Thai Navy) and overlaid onto the 1:20,000 scale administrative boundary GIS (ESRI Thailand, Co Ltd). The projection's rectification was verified and adjusted, whenever needed, using up to the ground control points per square kilometer. To simulate the December 26, 2004 tsuami propagation, we use the decimal degree data on the Cartesian coordinate system to construct the model grid. In the Bay Bengal (72° to 102° E in longitude and 13° S to 23.5° N in latitude), we regrid the data using linear interpolation to produce the uniform grid with 1.85×1.85 km, which approximately corresponds to a 1 minute grid spacing, yielding 1793 by 2191 points. The time step for each simulation is set to 1.2 sec. For a special case, we constructed the smaller model grid in the Andaman sea of Thailand (91°to 101° E in longitude and 3.6° to 12° N in latitude) to study the tsunami phenomenon along the Andaman sea coast of Thailand and regrid the data using linear interpolation to produce the uniform grid with 0.643×0.643

km, which approximately corresponds to a quarter of minute grid spacing, yielding 2,017 by 2,383 points. The time step for each simulation is set to 0.5 sec

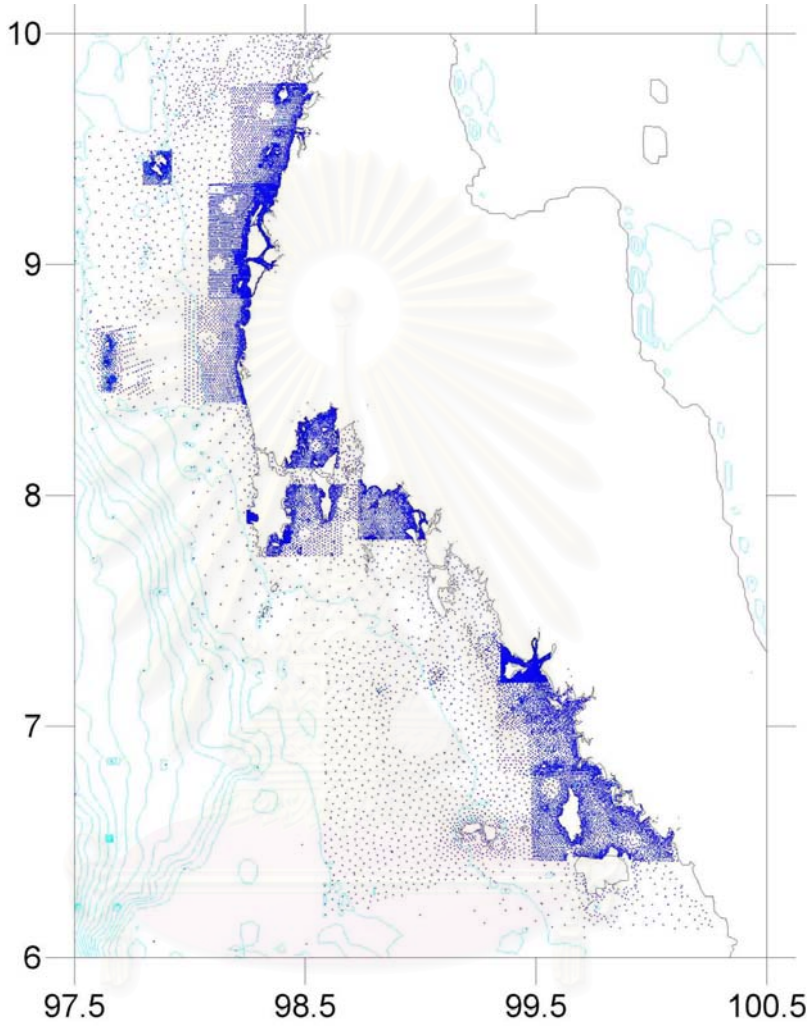

Figure 4.1: Bathymetry and Topography Data of Andaman Sea coast Thailand

4.2 Tsunami Source Parameters

Based on geophysical and seismological analyses, we identify five segments as shown in Figure 3.1 with different morphologies along the ruptured subduction zone. Segment 1 (L=220 km) covers the southern arc of the ruptured subduction zone, facing in a general SW direction (of tsunami propagation), perpendicular to rupture, and roughly extends

NW of the epicenter. The faulting trends North along two relatively sharp bends, one to the north and one two the south of the segment. Here, the overriding plate is at its steepest, and the water depth is largest along the ruptured subduction zone, at around h=5,100 m in the deepest part of the Java trench. Segments 2 and 3 cover along (L=150 and 390 km) and relatively straight section of the subduction zone in a NNW direction along the trench. The most notable feature is the nearly uniform profile of the overriding plate in the northern segment 3, with a steep rise from the subduction trench to a shallow ridge, followed by a descent into a deeper basin further East. The Southern, shorter and wider segment 2, covers the slip asperity, predicted off Banda Aceh in seismic inversion models, corresponding to a larger maximum slip responsible for the largest coastal runups measured in and around Banda Aceh. Direct effects of this large slip in the form of seafloor uplift may have been observed during the SEATOS cruise in the so-called "ditch"feature (Moran *et al.*, 2005). Segments 4 and 5 (L=150 and 350 km) feature a marked change in orientation and shape, notably a widening of the distance between the subduction zone and the basin to the east. The basin is narrower here, more in the form of the trench. The ridge is shallow enough to form a number of small islands. Segment 4 is facing Northern Thailand, where very large runup was measured, e.g., in Khao Lak. In Segment 5, a significant number of larger islands (the Andaman islands) are formed on the overriding plate (these are better visible in figure 4.2). These five segments are defined by individual location, shape, orientation, and slip, which the fault parameters for each segment given in Table 4.1. Figure 4.2 show the initial tsunami source, which computed with Okada's formula by using tsunami source parameters in Table 4.1.

Parameters	**Segment 1**	**Segment 2**	**Segment 3**	**Segment 4**	**Segment 5**
x_0 (longitude)	94.57	93.90	93.21	92.60	92.87
y_0 (latitude)	3.83	5.22	7.41	9.70	11.70
d (km)	25	25	25	25	25
φ (degree)	323	348	338	356	10
λ (degree)	90	90	90	90	90
δ(degree)	12	12	12	12	12
Δ (m)	18	23	12	12	12
L (km)	220	150	390	150	350
W (km)	130	130	120	95	95
μ (Pa)	4.0×10^{10}	4.0×10^{10}	4.0×10^{10}	4.0×10^{10}	4.0×10^{10}
t_0 (s)	60	272	588	913	1273
M_0 (J)	1.85×10^{22}	1.58×10^{22}	2.05×10^{22}	0.61×10^{22}	1.46×10^{22}
λ_0 (km)	130	130	120	95	95
η_0 (m)	-3.27; +7.02	-3.84; +8.59	-2.33; +4.72	-2.08; +4.49	-2.31; +4.60
T_0 (min)	24.77	17.46	23.30	18.72	18.72

Table 4.1: Tsunami source parameters used in TOPICS for Okada's (1985)

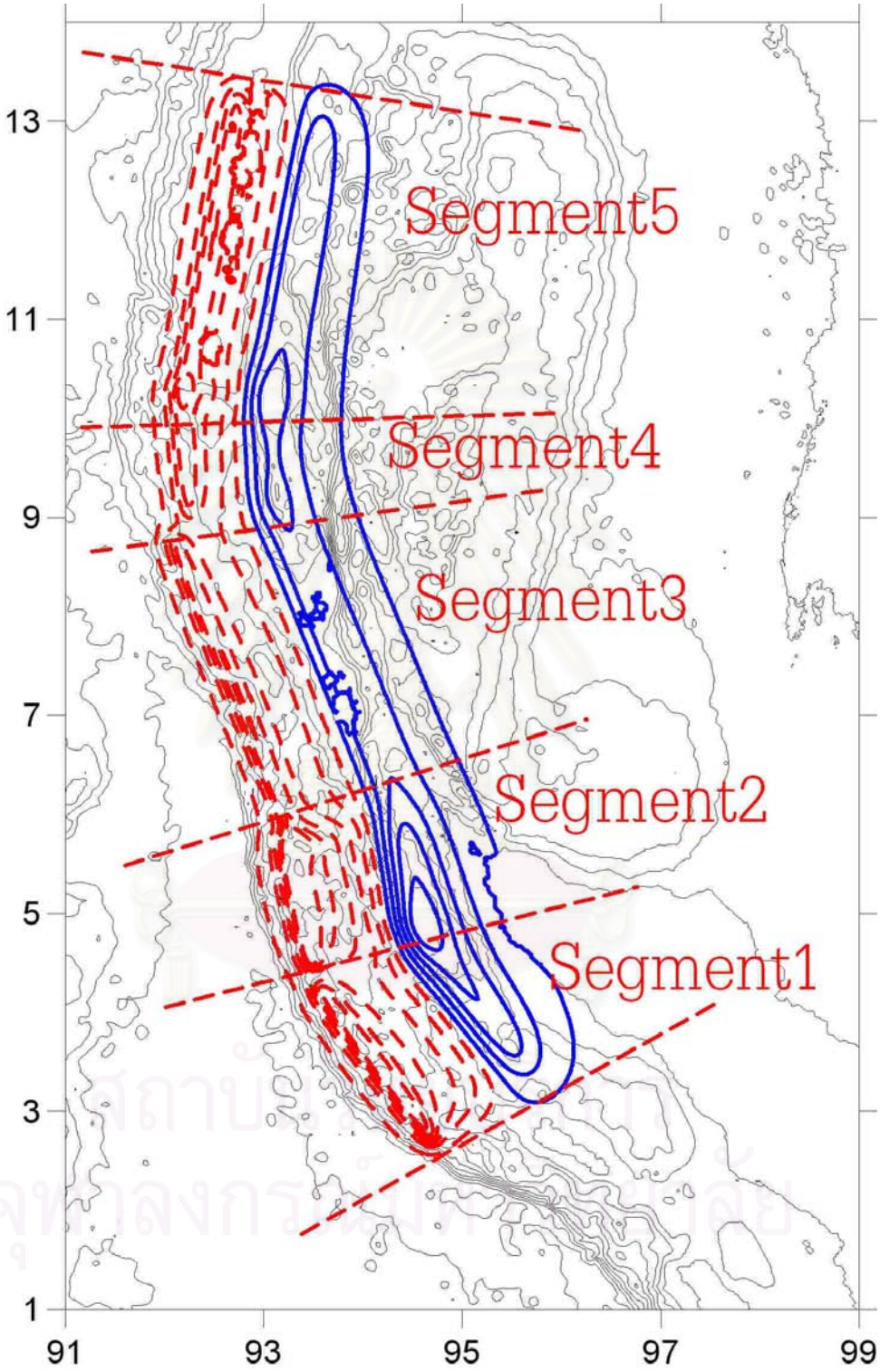

Figure 4.2: The initial tsunami source computed with Okada (1985) dislocation model; (– – –) represent uplift and (——) represent subsidence contours.

4.3 Tsunami Simulations

We perform the numerical simulations by combining source and wave propagation and inundation models into a single module referred to as Geowave, which the tsunami source is predicted by Okada's solution are to be used as an initial condition for the tsunami wave propagation and inundation model. In the simulations, the five segments of tsunami sources are triggered at the appropriate times t_0 according to the reduced speed of propagation of the rupture. Based on shear wave speed predicted by seismic inversion models (i.e. 0.87 km/s in the south and 0.70 km/s in the north, with an average shear wave speed of 0.8 km/s), the delay between each segments can be estimated and the values t_0 are provided in Table 4.1.

A composite fourth-order Adams Bashforth-Mounlton scheme (utilizing a third-order Adams-Bashforth predictor step and forth-order Adams-Moulton corrector step) and two kinds of boundary condition i.e. impermeable reflective vertical walls and transmitting or absorbing boundaries (Wei *et al.*, 1995) are used in numerical simulations (see Appendix III). In the last step of simulation, tsunami source have to be calibrated subject to available tide gage data. This is described in the next chapter.

CHAPTER V

DATA AND MODEL CALIBRATION

5.1 Data

5.1.1 Satellite Altimeter by Jason 1

The Jason 1 altimeter was launched in 2001 in a joint program between NASA and the French space agency CNES (Centry National D'Etudes Spatiales). Data plotted here are provided by the Radar Altimeter Database System of the Technical University of Delft, Holland (Gower, 2005).

On the December 26, 2004 during the tsunami event, the Jason1 altimetry satellite travelled on this cycle from 12° S and 20° N, between 2h 51' and 3h 02' UTC, or about two hours after the start of the event (Grilli *et al.*, 2006). It travelled about 1,500 km south of Sri Lanka, heading north-east towards the Bay of Bengal a above track 129 of its 254-track, 10-day pattern (Figures 5.1 and 5.2). This was the 109^{th} time the satellite had followed this track. Figure 5.3 shows that sea surface elevation during the tsunami event (cycle 109) and sea surface elevation about ten days before the tsunami event (cycle 108). The estimates of surface elevation measured along Jason1'satellite transect (Figure 5.4) was obtained along satellite track No. 129, by calculating the difference between the anomaly of the sea suface elevation for cycle 109 and 108 (Gower, 2005; Kulikov, 2005).

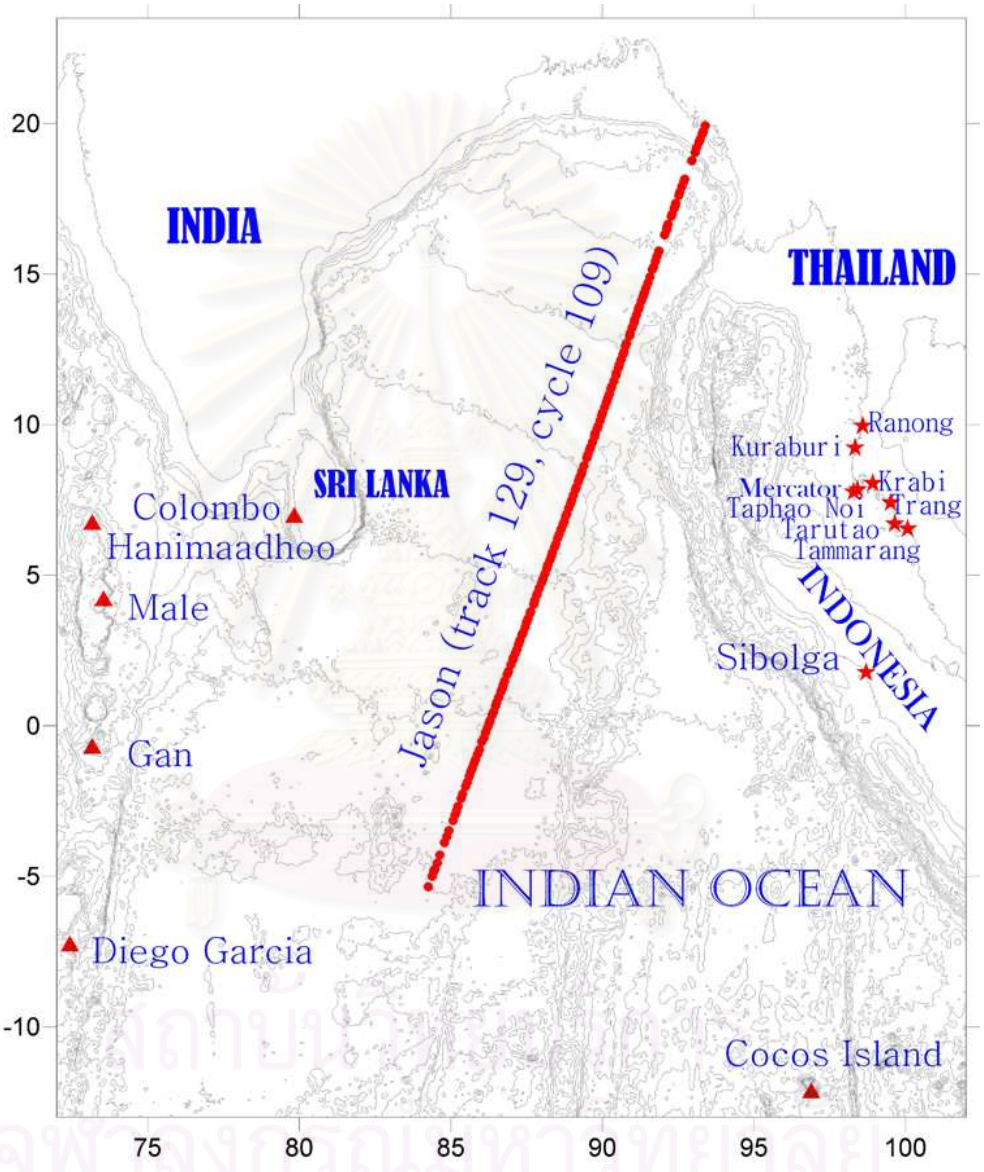

Figure 5.1: Numerical Domain, Tide gage location and Jason1 satellite altimetry (track 129, cycle 109)

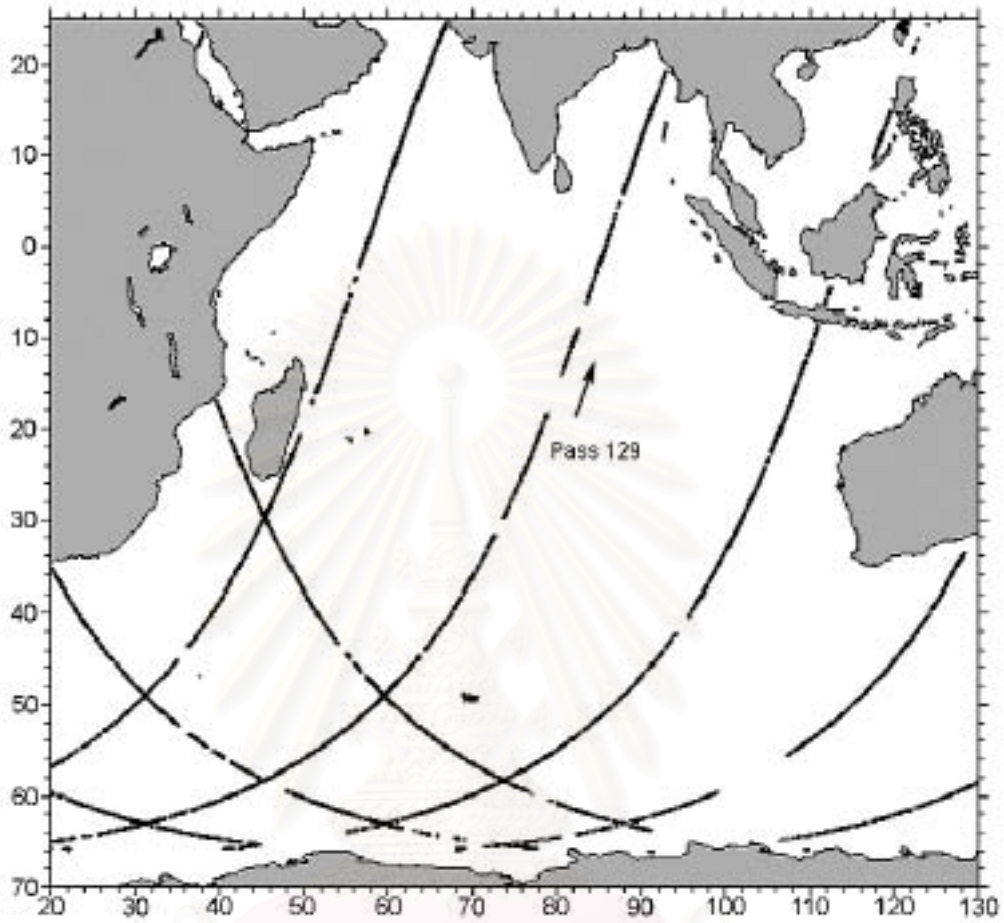

Figure 5.2: Track 129 and altimetry of Jason 1 (Gower, 2005)

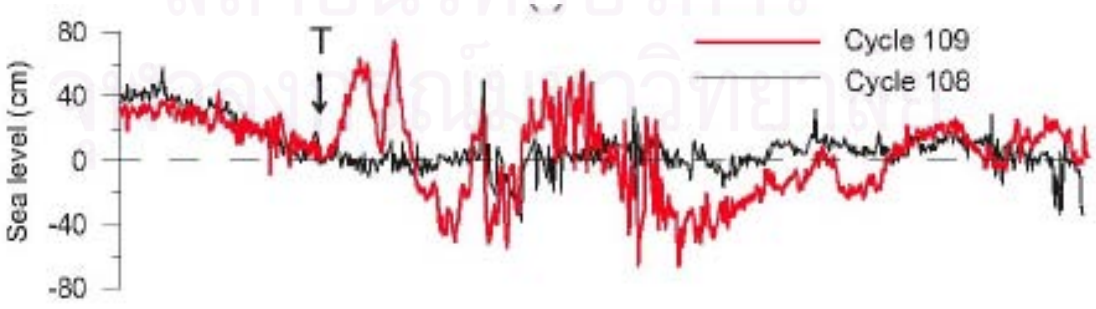

Figure 5.3: Jason 1 altimetry for cycles 108 and 109 along track 129 (Kulikov, 2005)

5.1.2 Tide Gages

During the tsunami event, tsunami elevations were measured at various coastal tide gages in the Indian Ocean (Merrifield *et al.*, 2005). In the study, we use 13 locations marked in Figure 5.1, for which accurate digital data was available. Data shown in Figure 5.5 is for 3 tide gages in the Maldives (Hannimaadhoo, Male, Gan; the northern two being in direct line of sight along the main direction of tsunami propagation from the source), Diego Garcia, South of the Maldives, Columbo, on the sheltered west side of Sri Lanka, Cocos island, directly south of the tsunami source, and the last seven tide gages (Taphao Noi, Kuraburi, Ranong, Pak Nam Krabi, Kantang, Tammarang and Tarutao) on the Andaman sea coast of Thailand. In addition, the tsunami was recorded with a depth echosounder by the Belgian yacht "Mercator", which was anchored 1 mile off Nai Harn Bay (SW of Phuket), in approximately 12 m under water at the time of the event. Tables 5.2 and 5.3 lists the tide gage and yacht names and their approximate locations. In Figure 5.5, the actual data points are marked by circles. Note that, for the first six tide gages, measured elevations were filtered by applying a moving average over a 120, 240, 240, 360, 120 and 60 s time window (Grilli *et al.*, 2006), that provided by UHSLC. For the five tide gages i.e. Taphao Noi, Ranong, Pak Nam Krabi, Kantang, and Tarutao, the estimates of surface elevation are obtained by calculating the difference between the $11^{\mathtt{th}}$ degree polynomial fitting for the predicted tide (Hydrographic Department of the Royal Thai Navy) and actual data of each tide gage. That is

$$y = a_0 + a_1x + a_2x^2 + a_3x^3 + a_4x^4 + a_5x^5 + a_6x^6 + a_7x^7 + a_8x^8 + a_9x^9 + a_{10}x^{10} + a_{11}x^{11}$$

where y represents surface elevation, x denotes time, and a_i, $(i = 0, 1, 2, ..., 11)$ are coefficients, shown in Table 5.1.

The low past filtering scheme (Hanning filter) is used to remove the low frequency signal in the last two tide gages: Kuraburi and Tammarang.

	Taphao Noi	**Krabi**	**Kantang**	**Ranong**	**Tarutao**
a_0	-2.74×10^{-4}	2.80	3.20	3.10	8.54×10^{-1}
a_1	3.33×10^{-1}	-6.16×10^{-1}	-4.08×10^{-1}	-3.68×10^{-1}	-6.72×10^{-1}
a_2	-5.44×10^{-1}	3.21×10^{-1}	2.59×10^{-2}	-2.71×10^{-1}	2.49×10^{-1}
a_3	1.30×10^{-1}	-2.88×10^{-1}	-2.11×10^{-2}	3.20×10^{-2}	-1.68×10^{-1}
a_4	-4.69×10^{-3}	1.44×10^{-1}	-9.09×10^{-3}	1.88×10^{-2}	5.61×10^{-2}
a_5	-2.24×10^{-3}	-2.30×10^{-2}	5.88×10^{-3}	-5.92×10^{-3}	-9.92×10^{-3}
a_6	4.36×10^{-4}	2.79×10^{-3}	-1.13×10^{-3}	8.76×10^{-4}	1.09×10^{-3}
a_7	-4.10×10^{-5}	-2.16×10^{-4}	1.11×10^{-4}	-8.18×10^{-5}	-8.00×10^{-5}
a_8	2.32×10^{-6}	1.08×10^{-5}	-6.35×10^{-6}	4.96×10^{-6}	3.94×10^{-6}
a_9	-7.96×10^{-8}	-3.42×10^{-7}	2.16×10^{-7}	-1.86×10^{-7}	-1.24×10^{-7}
a_{10}	1.52×10^{-9}	6.16×10^{-9}	-4.06×10^{-9}	3.90×10^{-9}	2.25×10^{-9}
a_{11}	-1.24×10^{-11}	-4.81×10^{-11}	3.27×10^{-11}	-3.46×10^{-11}	-1.76×10^{-11}

Table 5.1: Coefficients of 11^{th} degree polynomial fitting.

5.2 Model Calibration

In this study, we use the available tide gage data and anomalous water elevations in the Indian Ocean during the tsunami event, recorded by Jason's altimeter (track 129, cycle 109). These are discussed in the previous section and are used to calibrate the tsunami source model. Numerous iterations are performed until we obtain a best-fitted tsunami source. The iterative simulations concern the positions of the respective centroids, the strike angles and the rising time and tsunami mode of propagation in the calibration process to fit the tsunami arrival time and the amplitude. The comparison between numerical results with estimates of surface elevation measured along Jason1's satellite altimetry illustrated in Figure 5.4 shows satisfactory agreement, except for a small temporal shift at some locations. This may be due to the noises in satellite data. Table 5.2 lists the computed and observed arrival times of the tsunami at the gages defined as the time of the extremum of the first depression or elevation wave, whichever comes first (the first measured increase or decrease before the crest or trough). Figure 5.5 shows both measured and simulated time series in the Maldives (Hannimaadhoo, Male, Gan), Sri Lanka (Colombo), Diego Garcia, Cocos island, the Andaman sea coast of Thailand (Taphao Noi), and the yacht. The simulated tsunami usually arrives slightly too early, by up to 3 min., except as expected from above discussions on sphericity and Coriolis effects, at the two southern most locations, Diego Garcia and Cocos island, where the simulated tsunami arrives 16 and 11 min too early, respectively.

More specifically, in Figures 5.5a,b, we see that, except for a gage resolution effect, the agreement is good between simulations and observations at the two northern tide gages in the Maldives, Hannimaadhoo and Male, for the elevation and period of the first three waves. A good match is expected at these gages, as they lie on a fairly direct path of tsunami propagation, orthogonal to the source axis. At Gan, further south,

Figure 5.5c shows the agreement is reasonable for the first crest but not so good for later waves. However, this gage is located within a somewhat protected area, which yields a weaker signal quite affected by local coastal topography not resolved in the model. Except for a time shift, the agreement is reasonable at Diego Garcia for the first two waves in Figure 5.5d. In Columbo as shown in Figure 5.5e, the agreement for the first crest before the tide gage failed is quite good, particularly considering the tsunami had to propagate around the southern tip of Sri Lanka to reach the tide gage, very much like an edge wave. In Cocos island (Figure 5.5f), despite the southern location off the main direction of tsunami propagation, the agreement is quite good in amplitude and period for the first three waves, except for a time shift. The tide gage in Cocos island is located inside a lagoon in shallow water, and part of the time shift can be explained by the poor representation of slowing-down effects of waves in very shallow water in the model. In Taphao Noi, east of Phuket in southern Thailand, a depression wave first arrives, as expected, and the agreement is quite good in amplitude and period for the first two waves. Finally, in Figure 5.5h, we see that the yacht Mercator also experienced an initial depression wave, followed by three waves of elevation. The yacht was anchored near areas of Thailand that experienced very large waves and runup. The depression wave in the model arrives 1h49 min after the earthquake, only 1 min after that measured on the yacht, and its amplitude is in good agreement. The first crest elevation is also well predicted, but with a slight time shift in the period, and so is the third crest with a larger time shift. The second crest, however, is almost entirely missing from these simulations. At this stage it is fair to state that the Mercator signal is not fully explained yet in these simulations, beyond the first wave.

In the study, we perform model calibration for eastern side of the tsunami source by using seven tide gages along the Andaman sea coast of Thailand (Taphao Noi, Ranong, Kuraburi, Pak Nam Krabi, Kantang, Tammarang, and Tarutao) and the yacht. For

this case, we use a quarter minute grid spacing in the numerical domain. As previously mentioned these data are less reliable and thus must be taken with more caution, in particular for the arrival time. The sequence of waves and periodicity also are not as reliable as western data sets because the records are analogic. Besides, most of the eastern tide gages are located in river estuaries which is not an easy task to reproduce considering the 463 m grid spacing. We have imposed a lower weight to the present data compared to the ones of the western side which fit very well with the simulation results. Table 5.3 lists the details on the analogic tide gage records obtained from the Thai Habor Dpt.(THD) and the Hydrographic Dpt. of the Royal Thai Navy (HDRTN). The actual depths are unknowns and we report here the depth at the nearest computational node. The position of the MERCATOR yacht is not known with precision: it has been placed approximately 1.8 km off Nai Harn Bay where water depth is 12 m. The calibration results for this side are shown in Figure 5.6.

Locations	**Position** (Lat.,Long.)	**Model arrival time**	**Data arrival time**	**Depth** (m)
Hannimaadhoo, Maldives	(6.767, 73.167)	3h39'	3h40'	5
Male, Maldives	(4.233, 73.540)	3h26'	3h25'	4
Gan, Maldives	(-0.667,73.172)	3h25'	3h28'	5
Diego Garcia	(-7.233,72.435)	3h39'	3h54'	5
Columbo, Sri Lanka	(7.000, 79.835)	2h56'	2h59'	5
Cocos Island	(-12.133,96.877)	2h16'	2h27'	5
Taphao Noi, Thailand	(7.833, 98.417)	2h15'	2h18'	5
Mercator (Phuket), Thailand	(7.733, 98.283)	1h49'	1h48'	12

Table 5.2: Comparison of simulated and observed tsunami arrival time at tide gages and the yacht (Figure 5.1). The gage locations are fitted to the nearest grid points.

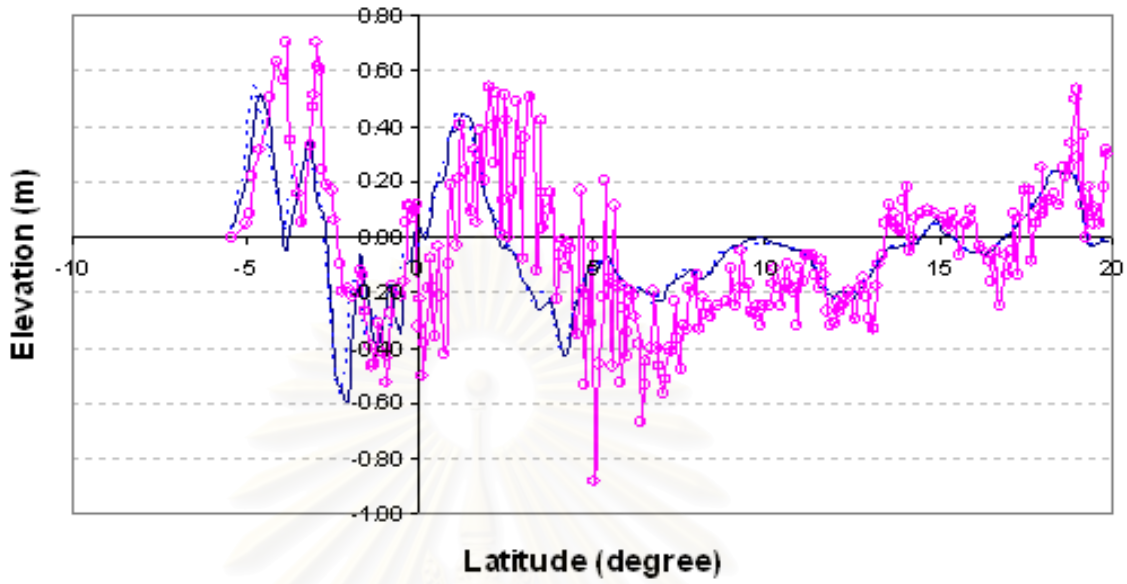

Figure 5.4: Comparison of tsunami elevation measured with satellite altimetry by Jason1 (—○—)and results of tsunami simulation with: Boussinesq wave model (——); Nonlinear Shallow Water wave model (– – –)

Locations	**Position**	**Owner**	**Depth**
MERCATOR (ME)	98.288°E ; 7.763°N	Private	12m
Kuraburi (Ku)	98.338°E ; 9.225°N	THD	3.8m
Taphao Noi (Tn)	98.422°E ; 7.833°N	HDRTN	5m
Krabi (Kr)	98.926°E ; 8.050°N	THD	3.4m
Kantrang (Ka)	99.514°E ; 7.404°N	THD	1.2m
Tarutao (Ta)	99.648°E ; 6.700°N	HDRTN	2.6m
Ranong (Ta)	98.590°E ; 9.950°N	HDRTN	1.9m
Tammarang (Tm)	100.076°E ; 6.533°N	HDRTN	3m

Table 5.3: Details on the analogic tide gage records obtained from THD and HDRTN and the MERCATOR yacht. The gage locations are fitted to the nearest grid points.

a) Hannimaadhoo

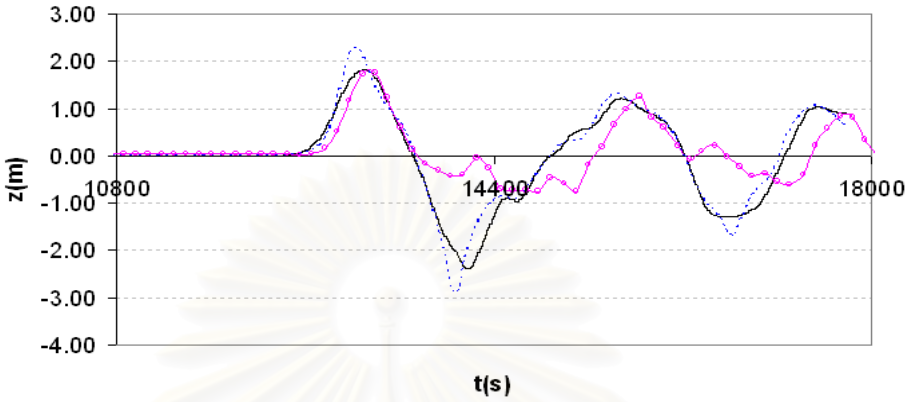

b) Male

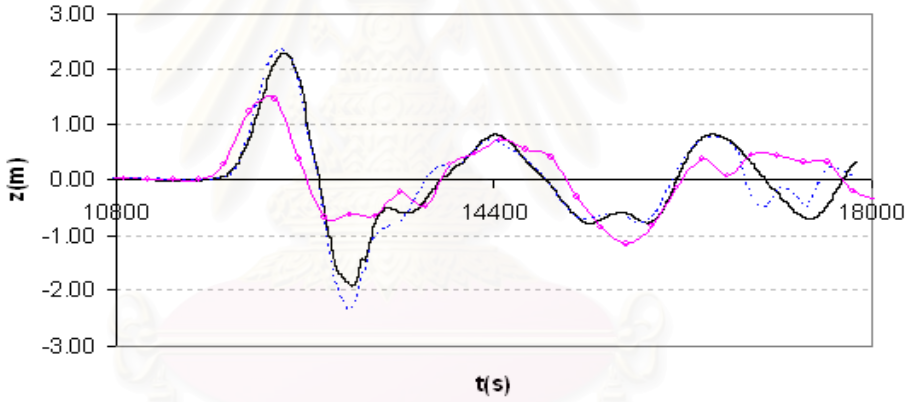

c) Gan

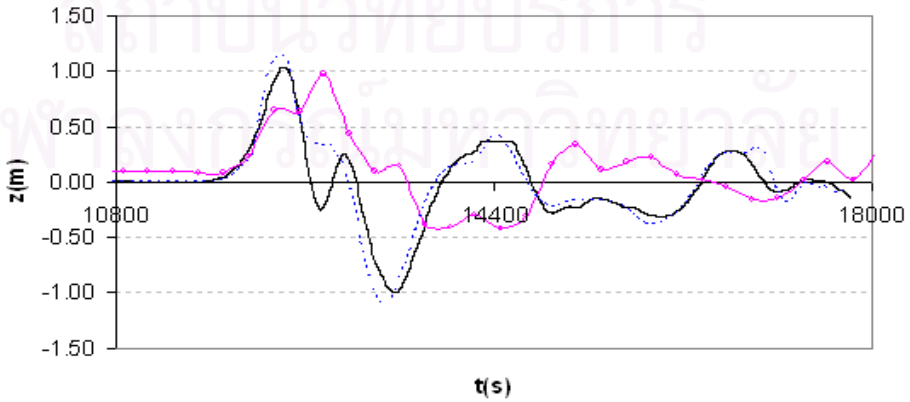

d) Diego Garcia

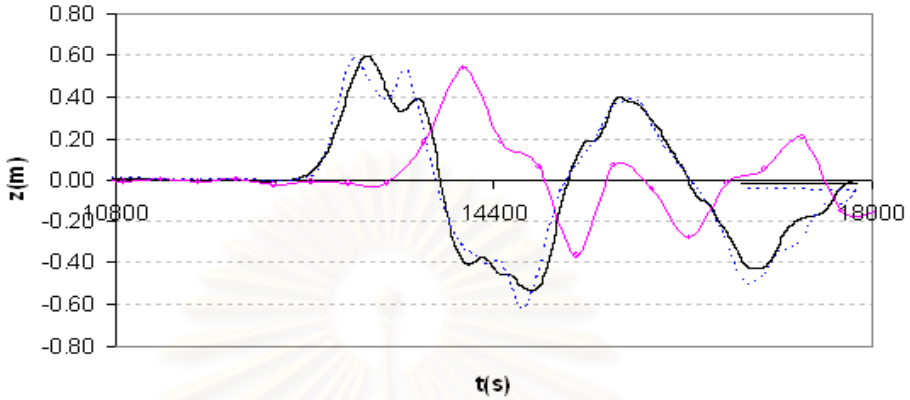

e) Colombo

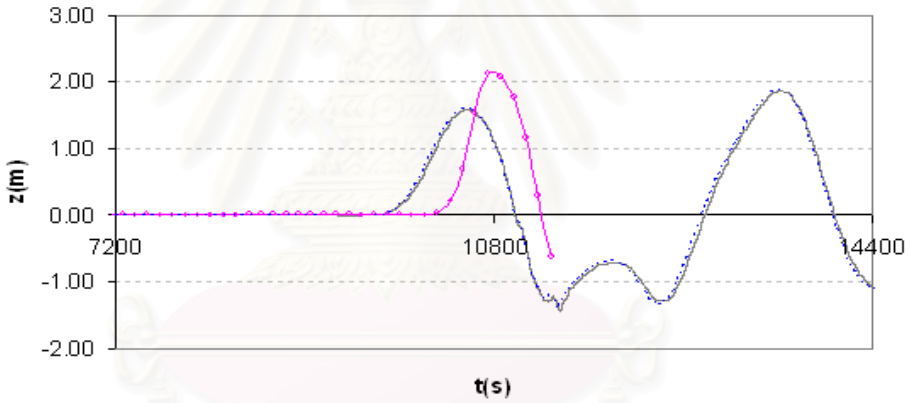

f) Cocos Island

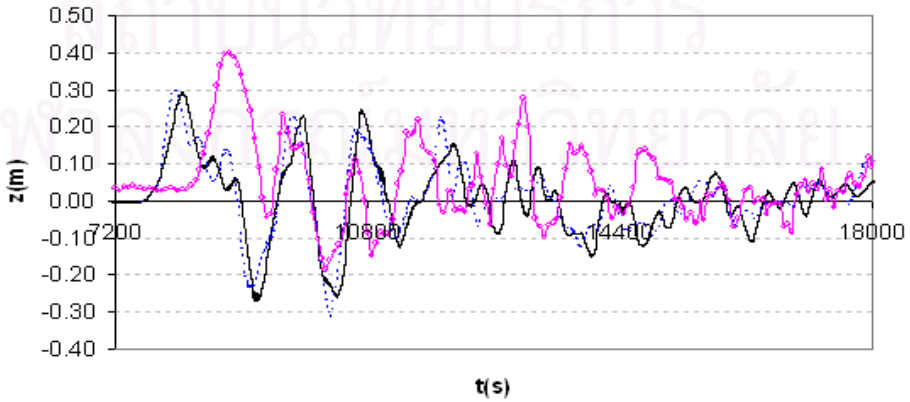

g) Taphao Noi

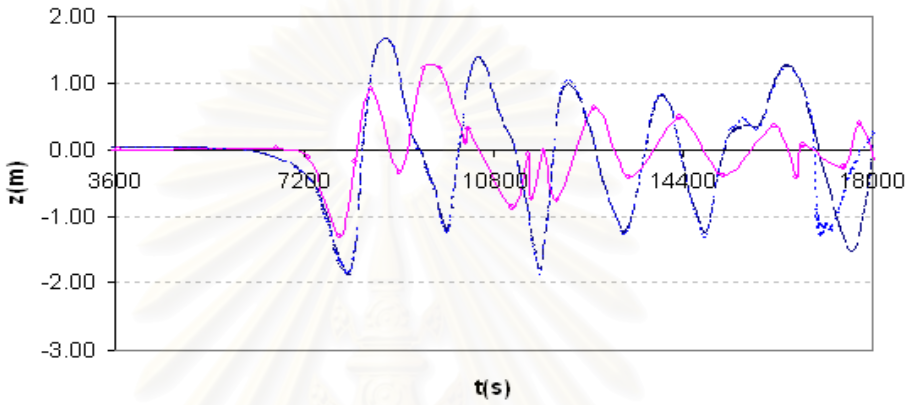

h) Mercator yacht

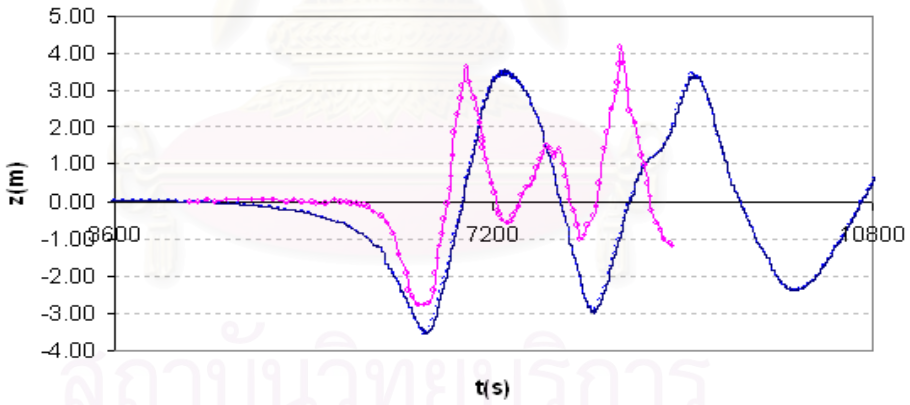

Figure 5.5: Comparison of tsunami elevation measured (—∘—) with Boussinesq wave model (——); Nonlinear Shallow Water wave model (– – –), at the tide gages and the yacht, marked in Figure 5.1 for 1 minute grid spacing domain

a) Taphao Noi

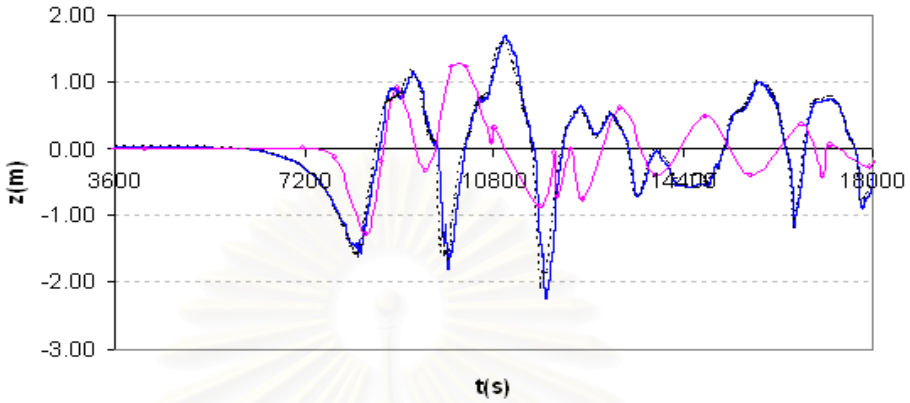

b) Tarutao

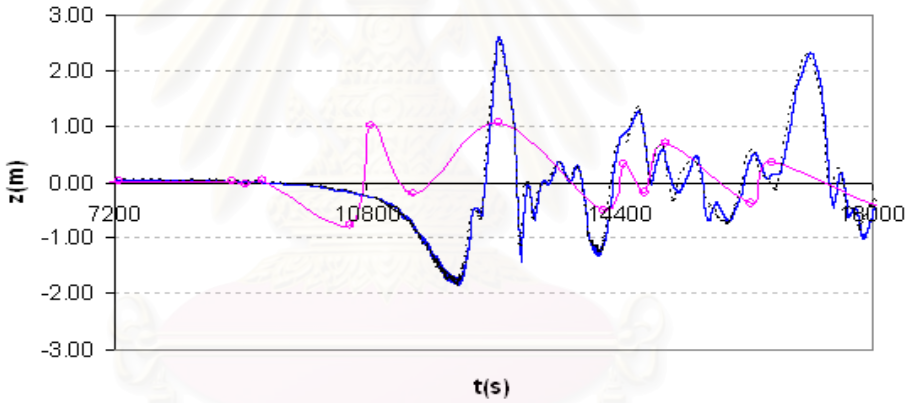

c) Pak Nam Krabi

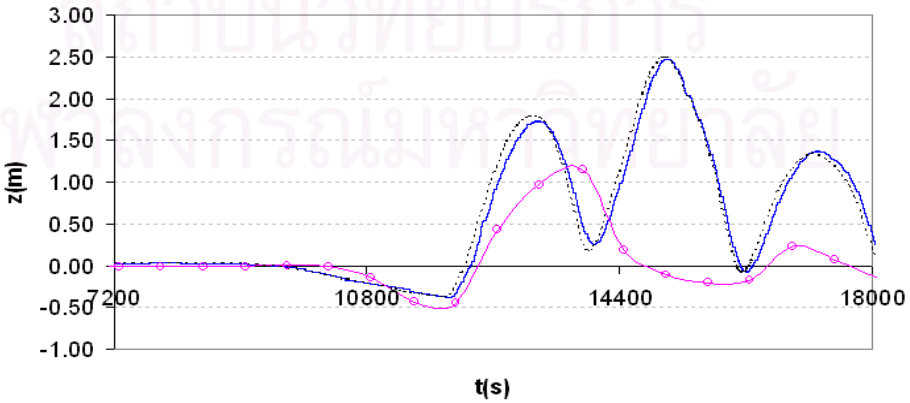

d) Kuraburi

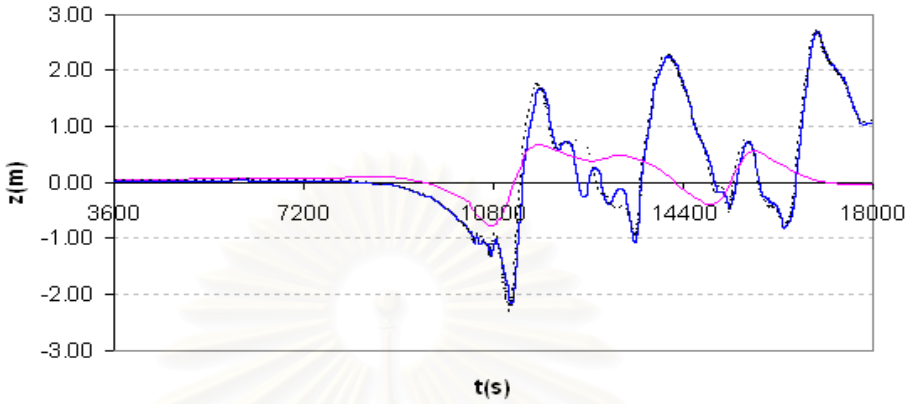

e) Ranong

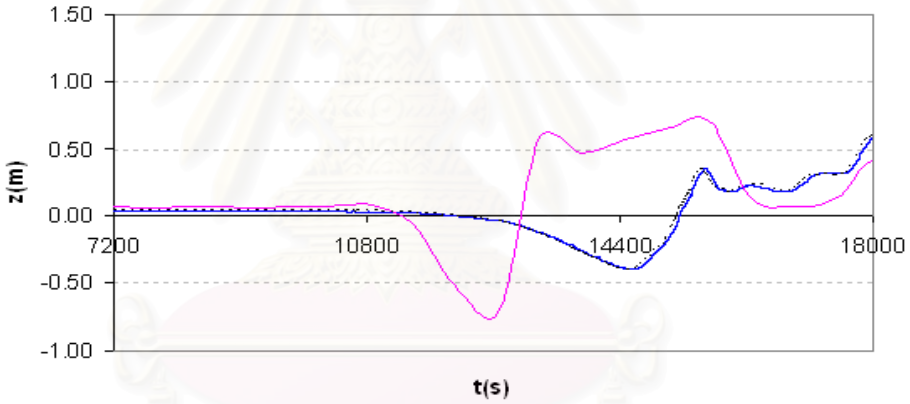

f) Kantang

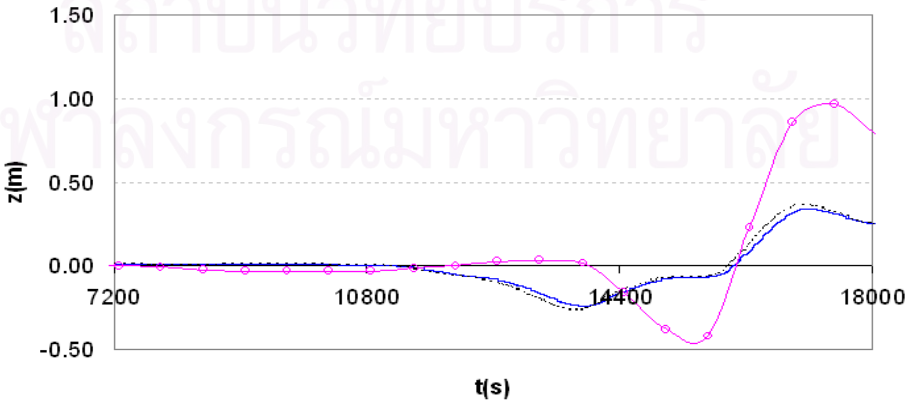

g) Tammarang

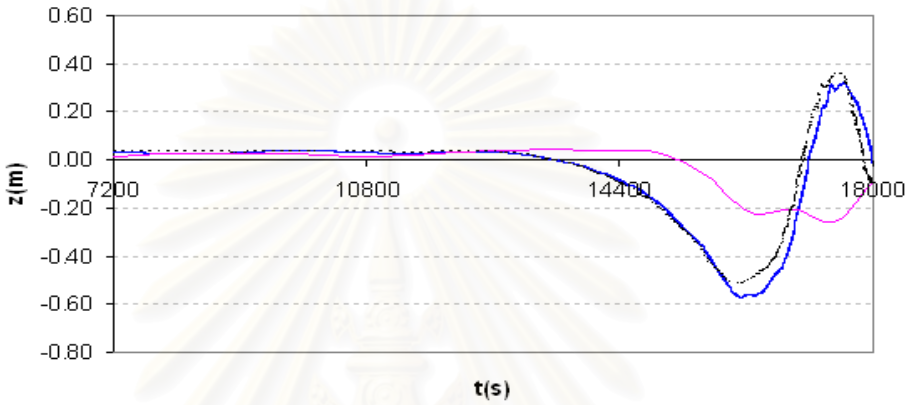

h) Mercator yacht

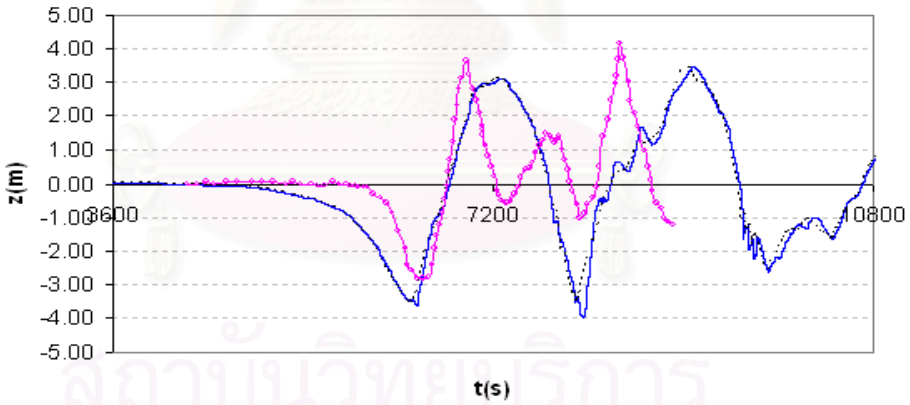

Figure 5.6: Comparison of tsunami elevation measured (—○—) with Boussinesq wave model (——); Nonlinear Shallow Water wave model (– – –), at the tide gages and the yacht, marked in Figure 5.1 for a quarter minute grid spacing domain

CHAPTER VI

NUMERICAL RESULTS AND DISCUSSION

The maximum wave heights above the sea level are plotted in Figure 6.1 showing the tsunami's radiation patterns. This shows that there are largest runups near Banda Aceh in northern Sumatra, along the Andaman coastline of Thailand, around the Nicobar-Andaman islands, and on the eastern side of India and Sri Lanka. Detail of maximum elevations in the regional area of Banda Aceh is depicted in Figure 6.2.

As shown in Figure 6.2, the largest runups are predicted near Banda Aceh (northern Sumatra). The largest runup measured on the west coast of Banda Aceh are under-predicted by 50% due to the lack of detailed coastal bathymetry and topography. The runup however occurred through a combination of deep inland flooding and tsunami interaction with complex topographic features, which focused waves and enhanced runup. Such features are not acculately represented in the ETOPO2 data set (Satake *et al.*, 2006) and are not resolved well enough in the 1 minute grid spacing.

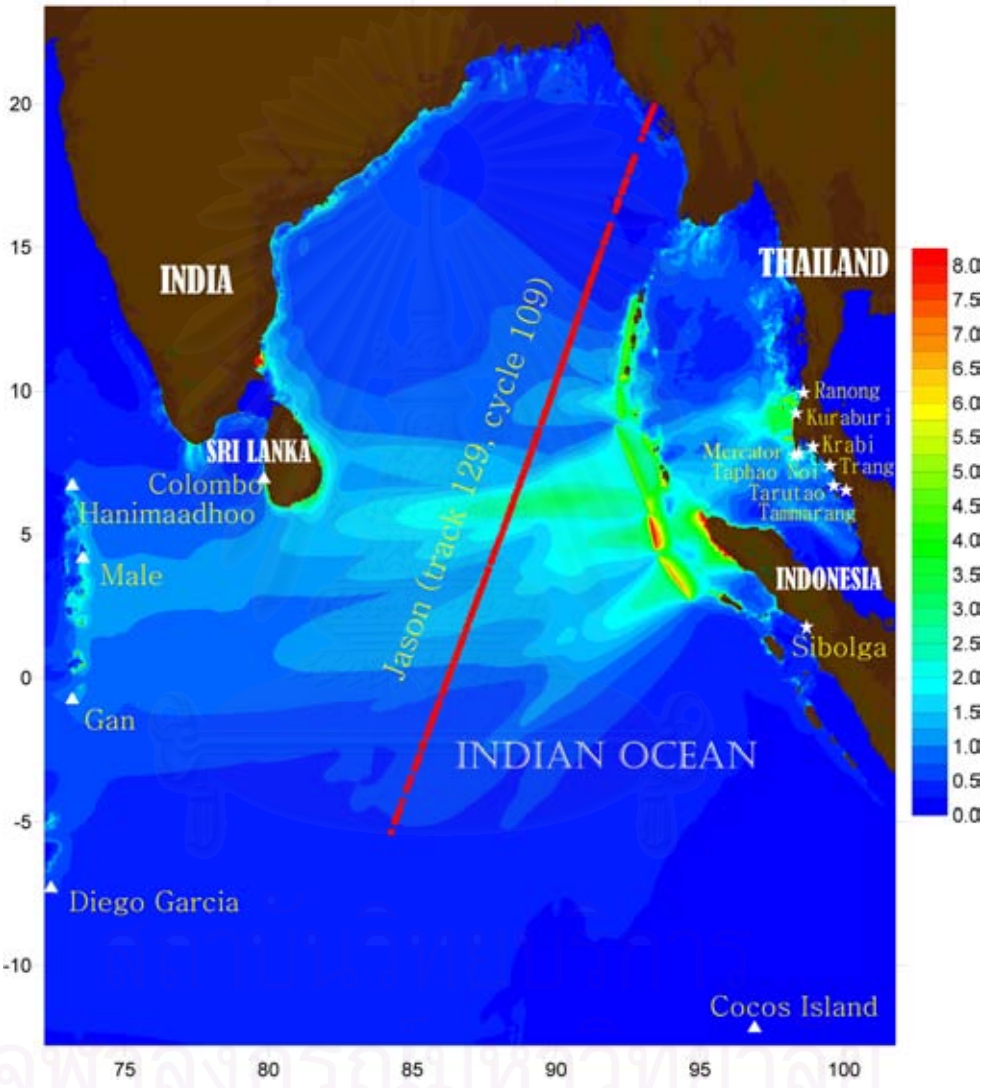

Figure 6.1: Maximum elevations in Bay of Bengal

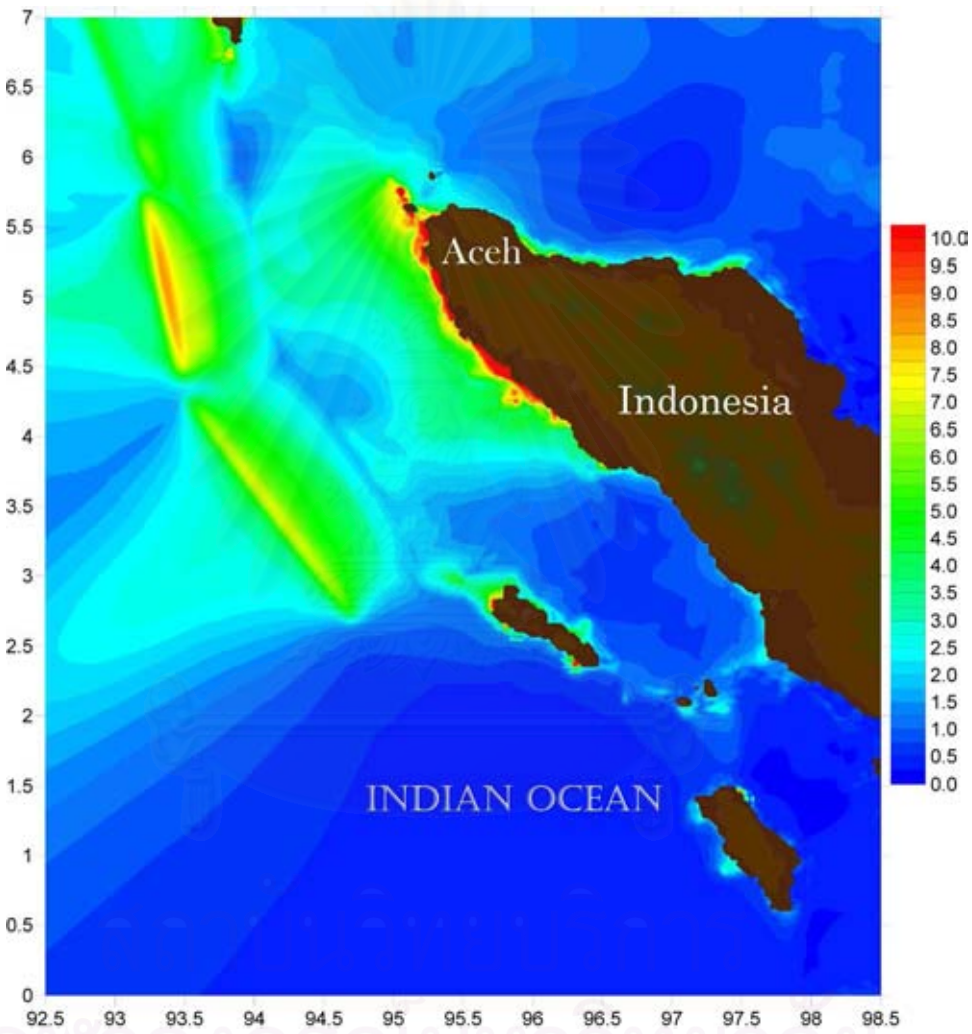

Figure 6.2: Maximum elevations along Banda Aceh of Indonesia

In the special case, we construct a quarter minute grid spacing on the smaller domain described in chapter 4 to simulated the maximum wave heights along the Andaman sea coast of Thailand. It is shown in Figure 6.3 that there is the better agreement on the extreme runup values along the westcoast of Thailand.

Finally we report the quantitative simulated runup map all along the coast of Thailand and compare to post-tsunami field surveys measurements (Figures 6.4, 6.5, and 6.6). The simulation reproduces nearly perfectly observations when available all along the Andaman coast. It is fair to say that all available updated observations have been reported in the Figures. The simulated runups also reproduce all local abrupt variations (e.g., in Khao Lak, near Sarasin bridge, in Patong beach, in the southern coast of Phuket island). The overall excellent fit of the runup amplitude and along the coast gradient states that the simulation is highly coherent.

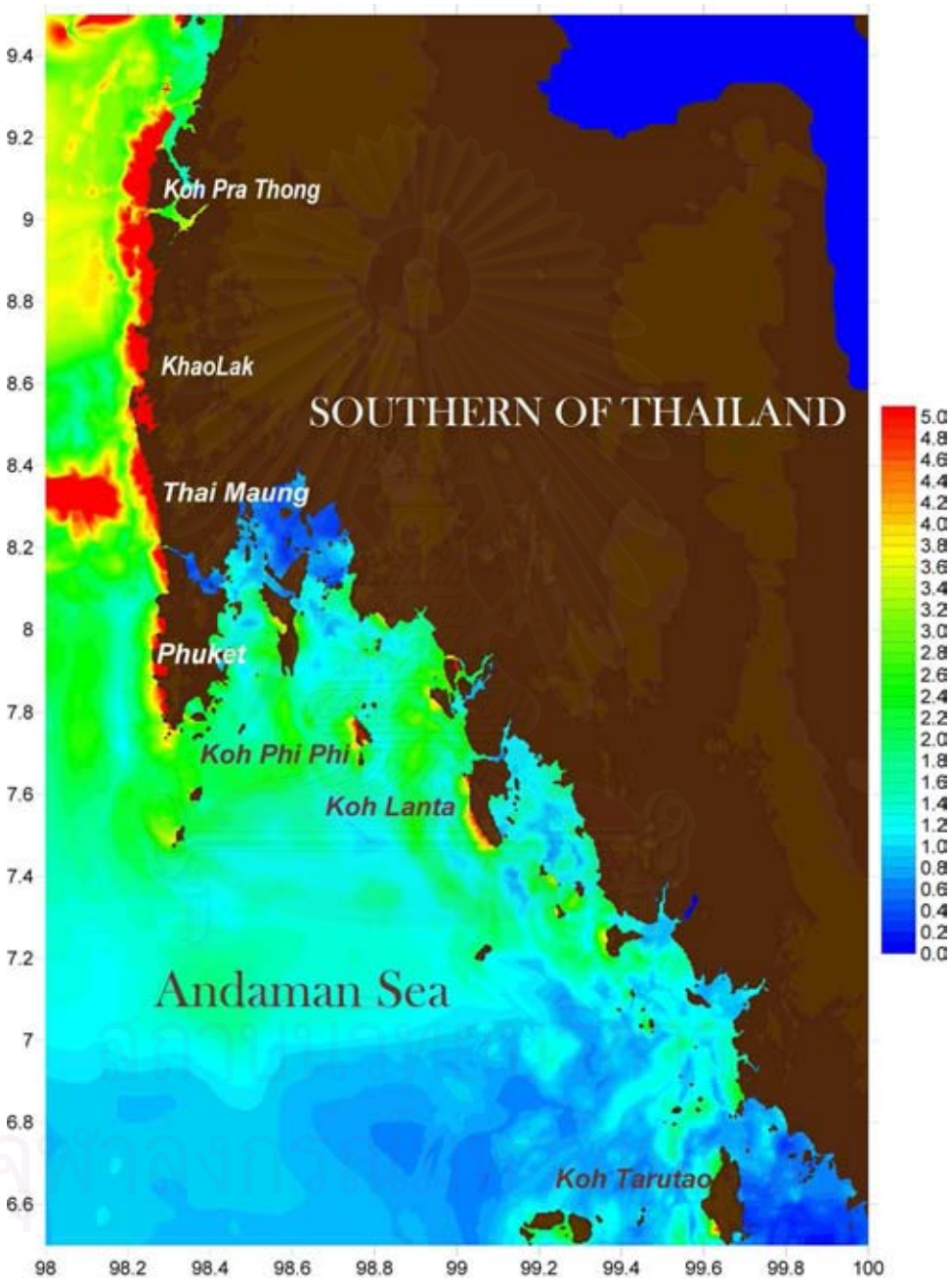

Figure 6.3: Maximum elevations along the westcoast of Thailand

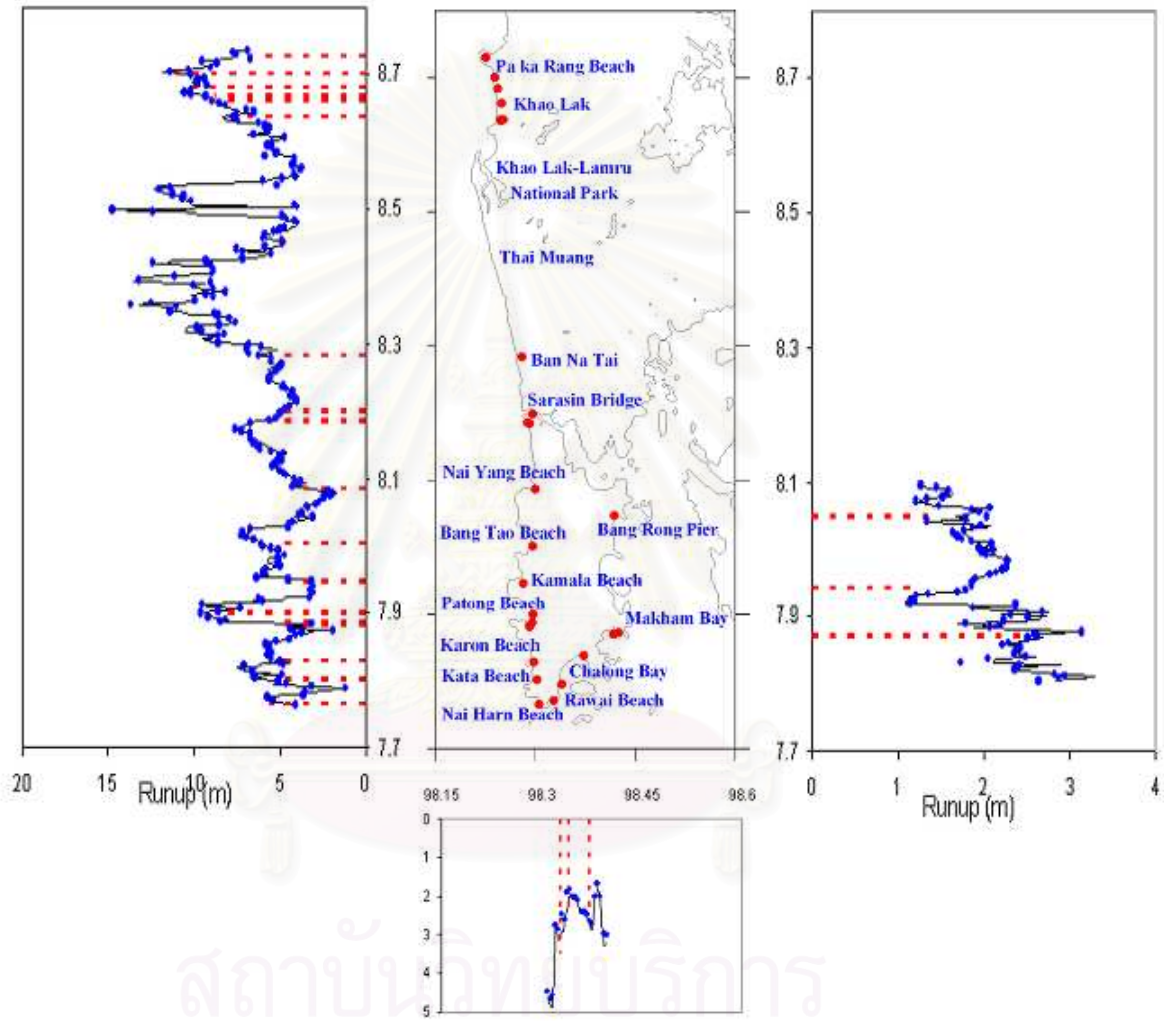

Figure 6.4: Comparison of simulated and observed data for runup along westcoast of Khao Lak and Phuket of Thailand: (– – –) for observation; (——) for Boussinesq model; (• • •) for Nonlinear Shallow Water wave model

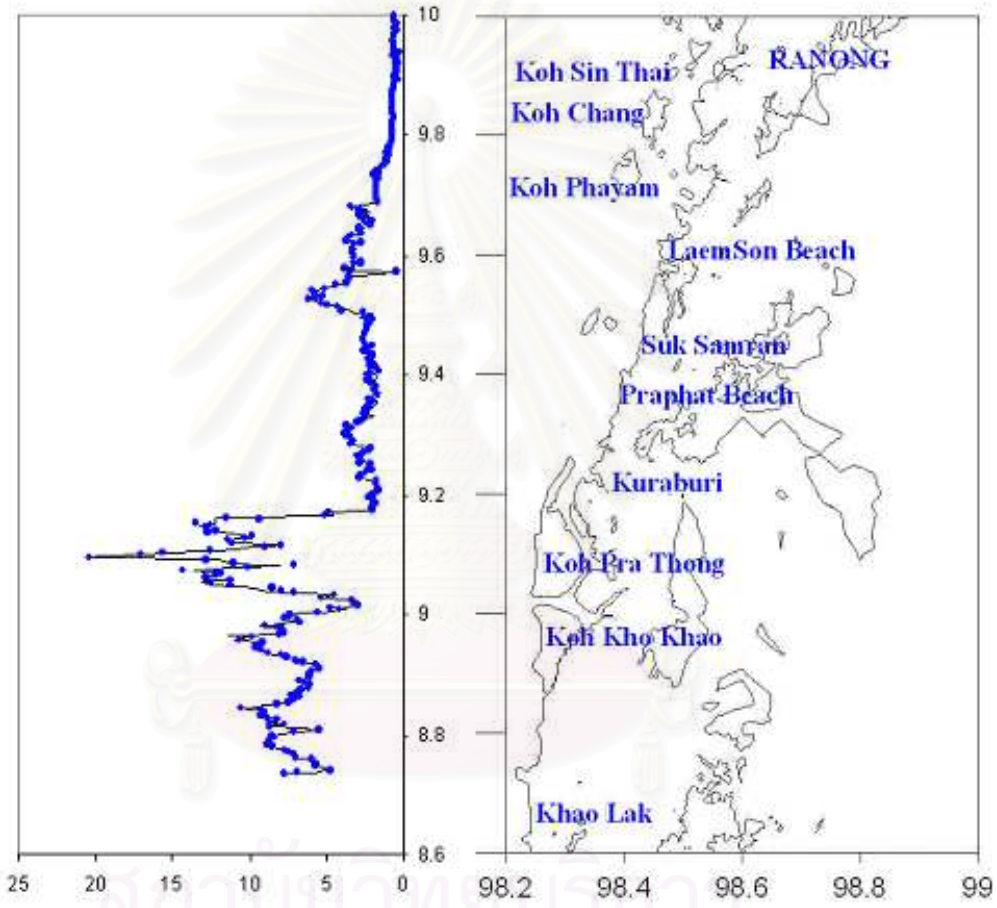

Figure 6.5: Simulated runup along westcoast of Ranong and Phang Nga of Thailand: (——) for Boussinesq model; (• • •) for Nonlinear Shallow Water wave model

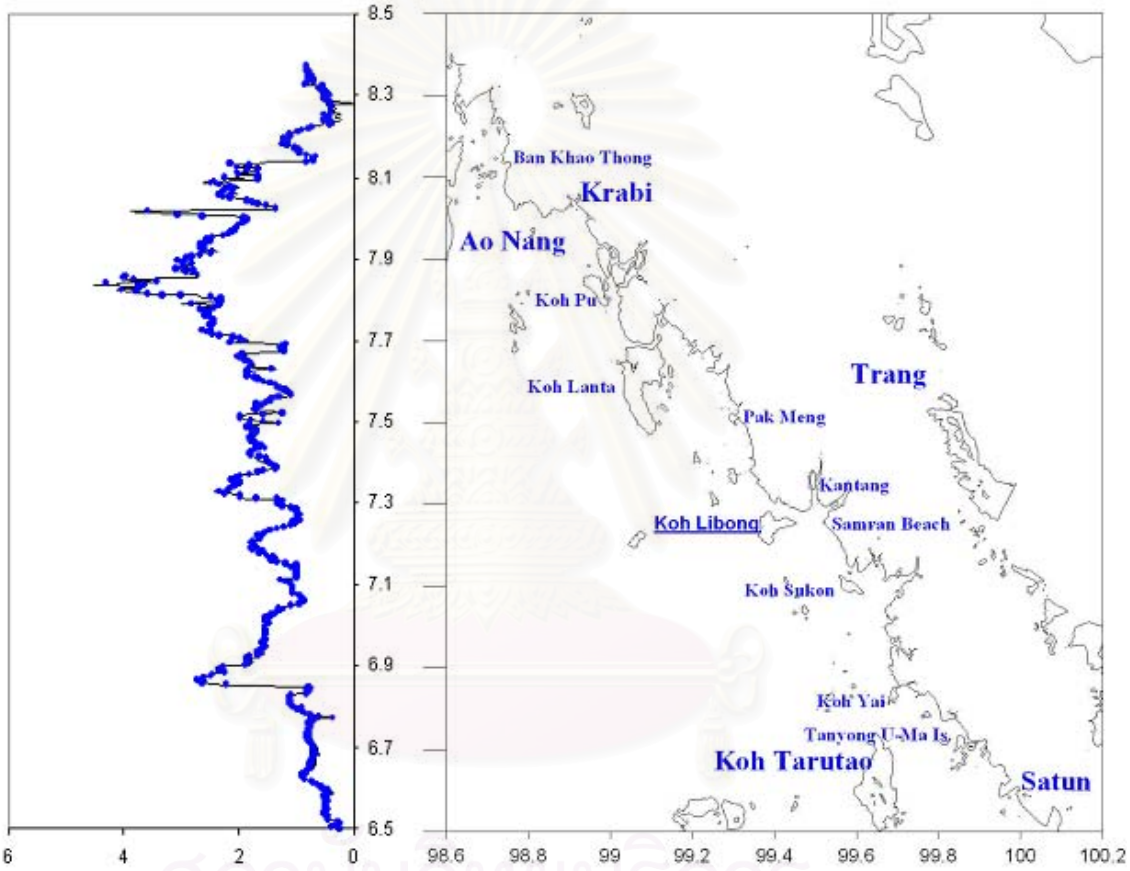

Figure 6.6: Simulated runup along westcoast of Krabi, Trang and Satun of Thailand: (——) for Boussinesq model; (• • •) for Nonlinear Shallow Water wave model

To estimate dispersive effects, the same simulation is performed by using the fully nonlinear wave model (FUNWAVE) to solve the nonlinear shallow water wave equations (NSWE). Both grid data and numerical methods are identical. Surface elevations are calculated along the satellite transect with the NSWE model and plotted in Figure 5.4. Differences with FUNWAVE results are mainly visible in the south of the equator. In NSWE results, as expected, the first peak of the leading wave is sligthly higher and steeper, while the second peak is much smaller (almost half trough to crest height) than in Boussinesq model results. The same is true for the third and fourth peak in the wavetrain, with the latter almost disappearing in NSWE results. Surface elevations at tide gages are calculated as well using the NSWE model and plotted in Figures 5.5 and 5.6. In the far distant Maldives, in Figure 5.5a, b, c NSWE results overpredicts both the first crest and trough in the tsunami wavetrain, with some of the secondary oscillations even disappearing (Gan). Similar observations can be made for Diego Garcia and Cocos island. Surprisingly, there is almost no difference for Columbo, maybe because, for a large part of its propagation, the tsunami propagates around the southern tip of Sri Lanka, in the manner of an edge wave, in shallow water (i.e., without dispersion; this can be clearly seen in animations of model results). For Taphao Noi, Ranong, Kuraburi, Pak Nam Krabi, Kantang, Tammarang, Tarutao and the Mercator yacht in Thailand (Figures 5.5g, h and 5.6), NSWE and Boussinesq results are almost identical, likely because the tsunami propagation distance in deep water is rather short (east of the source), and the tsunami is essentially non dispersive in shallow water.

CHAPTER VII

CONCLUSION

In this study, we construct a tsunami source consisted of five properly parameterized dislocations sources (Okada, 1985), for the December 26, 2004 tsunami by using a variety of seismological, geological, seafloor morphology, and tsunami elevation constraints. These sources simulate the co-seismic bottom deformation, caused by the earthquake, that propagated along 1,200-1,300 km length of rupture zone of the Andaman-Sunda trench. Our seafloor deformation agrees well with predictions of seismic inversion models as well as GPS data. We have simulated the tsunami event by specifying the 5 dislocation sources as a time sequence of free surface elevations (lasting about 1,200 s) in a wave propagation and inundation model (fully nonlinear Boussinesq wave model). We have also constructed the model grid by using ETOPO2 bathymetry and topography data together with denser and more accurate digitized bathymetry and topography data along the Andaman sea coast of Thailand (1 minute grid spacing to simulated the tsunami affect in Bay of Bengal and a quarter minute grid to simulate tsunami in the Andaman sea of Thailand). We found reasonable agreement between model simulations and measured elevations at shallow water tide gages around Indian Ocean, a deep water satellite transect, and observed runup values at many shoreline locations. Considering the data available at the present stage and the small differences between observed and simulated tsunami elevations and timing, it is believed that a reasonable and ad hoc source for the December 26, 2004 event has been properly proposed. To estimate dis-

persive effects, FUNWAVE can be set to perform the simulations under the Nonlinear Shallow Water Equations (NSWE) for the same set of parameters. It is found that, in the regions of deeper water in WSW direction of main tsunami propagation west of the source, the dispersion can reduce the wave amplitude by up to 20% compared to the nondispersive shallow water equation model (Grilli *et al.*, 2006). These differences decrease significantly after the tsunami has reached the shallower continental shelf.

Finally, to improve the model, effects of sphericity should be included in the numerical model. We believe spherical effects could help explain some of the differences in arrival time observed at the tide gages as compared with our simulation results.

References

Ammon, C.J. *et XII alia.* (2005). "Rupture process of the 2004 Sumatra-Andaman earthquake." *Science*, 308, 1133-1139.

Chen, Q., Kirby, J.T., Dalrymple, R.A., Kennedy, A.B. and Chawla, A. (2000). "Boussinesq modeling of wave transformation, breaking, and run-up. II: 2D", *J. Wtrwy, Port, Coast, and Oc. Engrg*, ASCE, 126(1), 48-56.

Day, S.J., Watts, P., Grilli, S.T. and Kirby, J.T. (2005). "Mechanical models of the 1975 Kalapana, Hawaii earthquake and tsunami.", *Marine Geology*, 215(1-2), 59-92.

Fritz, H.M. and Synolakis, C.E. (2005). "Field survey of the Indian Ocean tsunami in the Maldives." *Proc 5th Intl on Ocean Wave Meas and Analysis* (WAVES 2005, Madrid, Spain, July 2005), ASCE Publ, paper 219.

Gower. (2005). "Jason 1 detects the Dec. 26, 2004 tsunami." *Eos Trans. AGU*, 86(4), 37.

Grilli, S.T., Ioualalen, M., Asavanant, J., Shi, F., Kirby, J., and Watts, P. (2006). "Source constraints and model simulation of the December 26, 2004 Indian Ocean Tsunami.", submitted to *J Waterway Port Coast and Ocean Engng.*

Harada, K. (2005). "The December 26, 2004 Sumatra Earthquake, Tsunami Field Survey around Phuket, Thailand", `http://www.drs.dpri.kyoto-u.ac.jp/sumatra/thailand/phuket_survey_e.html`

Kawata, T. *et XIV alia.* (2005). "Comprehensive analysis of the damage and its impact on coastal zones by the 2004 Indian Ocean tsunami disaster." *Disaster Prevention Research Institute*, `http://www.tsunami.civil.tohoku.ac.jp/sumatra2004/report.html`

Kennedy, A.B., Chen, Q., Kirby, J.T., and Dalrymple, R.A. (1999). "Boussinesq modelling of wave transformation, breaking, and runup. I:1D." *J. Waterway Port Coast and Ocean Engng.*, (in press).

Kirby, J.T. (2003). "Boussinesq models and applications to nearshore wave propagation, surf zone processes and wave-induced currents.", *Advances in Coastal Modeling*, V.C. Lakhan (ed), Elsevier Oceanography Series 67, 1-41.

Kirby, J.T., Wei, G., Chen, Q., Kennedy, A.B. and Dalrymple, R.A. (1998). Fully Nonlinear Boussinesq wave model Documentation and User's Manual., *Research Report NO.CACR-98-06.*

Kulikov, E. (2005). "Dispersion of the Sumatra tsunami waves in the Indian Ocean detected by satellite altimetry.", Report from *P. P. Shirshov Institute of Oceanology*, Russian Academy of Sciences, Moscow.

Mei, C. C. (1989). The applied dynamics of ocean surface wave. *World Science.*

Merrifield, M.A. *et XXIII alia.* (2005). "Tide gauges observations of the Indian Ocean tsunami, December 26, 2004.", *Geophys. Res. Letters*, 32, L09603, doi:10.1029/2005GL022610.

Moran, K., Grilli, S.T. and Tappin, D. (2005). "An overview of SEATOS: Sumatra earthquake and tsunami offshore survey.", *EOS Trans. AGU*, 86(52), Fall Meet. Suppl., Abstract U14A-05.

Nwogu, O. (1993). "An alternative form of the Boussinesq equations for nearshore wave propagation.", *J. Waterway Port Coast and Ocean Engng.*, 119(6), 618-638.

Okada, Y. (1985). "Surface deformation due to shear and tensile faults in a half-space." *Bull. Seis. Soc. Am.*, 75(4), 1135-1154.

Satake, K. *et XI alia.* (2005). "Report on post tsunami survey along the Myan-

mar coast for the December 2004 Sumatra-Andaman earthquake." http://unit.aist.go.jp/actfault/english /topics/Myanmar/index.html

Satake, K. *et XI alia.* (2006). "Tsunami heights and damage along the Myanmar Coast form the December 2004 Sumatra-Andaman earthquake." *Earth Planets Space*, (in press).

Watts, P., Grilli, S.T., Kirby, J.T., Fryer, G.J., and Tappin, D. (2003). "Landslide tsunami case studies using a Boussinesq model and a fully nonlinear tsunami generation model." *Nat. Hazards and Earth Sci. Systems*, 3(5), 391-402.

Wei, G. and Kirby, J.T. (1995). "Time-dependent numerical code for extended Boussinesq equations." *J. Waterway Port Coast and Ocean Engng.*, 121(5), 251-261.

Wei, G., Kirby, J.T., Gilli, S.T., and Subramanya, R. (1995). "A fully nonlinear Boussinesq model for surface waves. Part 1. Highly nonlinear unstandy waves" *J. Fluid Mech.*, 294(5), 71-92.

Wells, D. L., and Coppersmith, K. J. (1994). "New empirical relationships among magnitude, rupture length, rupture width, rupture area, and surface displacement." *Bull. Seismological Soc. of America.*, 84, 974-1002.

APPENDICES

Appendix I

Derivation of fully nonlinear Boussinesq wave Equations

Following Wei *et al.* (1995) and Mei (1989),we use standard techniques to construct the fully nonlinear equations based on a series solution for Laplace's equation in the fluid domain.

We consider a three-dimensional wave field with water surface elevation $\eta(x, y, t)$, at time t, propagating over a variable water depth $h(x, y)$. A cartesian coordinate system (x, y, z) is adopted, with z measured upwards from the still-water level. The fluid is assumed to be inviscid and incompressible, and the flow is assumed to be irrotational.

To proceed, the appropriate scaling for the regime where wavelength exceeds water depth is chosen:

$$(x, y) = (k_0 x', k_0 y'), z = \frac{z'}{h_0}, t = \sqrt{g h_0 k_0^2}\, t', \eta = \frac{\eta'}{a_0}, \phi = \left(\frac{a_0\sqrt{g h_0}}{k_0 h_0}\right)^{-1} \phi'. \qquad \text{(A.1)}$$

Here primes denote dimensional variables, h_0 is a referenced water depth, a_0 is a referenced wave amplitude scale, and k_0 is an inverse horizontal length scale. The dependent variables are surface elevation η and velocity potential ϕ. Velocity components are defined by

$$\mathbf{u} = (u, v) = \nabla\phi \qquad \text{(A.2)}$$

for horizontal velocities, where $\nabla = (\partial/\partial x, \partial/\partial y)$, and

$$w = \phi_z \qquad \text{(A.3)}$$

for vertical velocity. The subscripts x,y,z, or t denote partial derivatives with respect to the corresponding variable. The resulting scaled problem is characterized by the dimensional ratios

$$\mu = k_0 h_0, \ \delta = a_0/h_0 \tag{A.4}$$

Parameter μ characterizes frequency dispersion, and the limit $\mu \to 0$ represents the nondispersive limit. The designation *weakly dispersive* refers to the regime $\mu \ll 1$. Parameter δ characterizes nonlinearity, and the limit $\delta \to 0$ represents the linear limit. The designation *weakly nonlinear* refers to the regime $\delta \ll 1$. In the present context, we use the terminology *fully nonlinear* to indicate that no truncation based on power of δ is employed in order to obtain the corresponding model equations. The resulting set of scaled equations is given by

$$\nabla^2\phi + \frac{1}{\mu^2}\phi_{zz} = 0, \qquad -h \le z \le \delta\eta \tag{A.5}$$

$$\nabla h \cdot \nabla\phi + \frac{1}{\mu^2}\phi_z = 0, \qquad z = -h \tag{A.6}$$

$$\eta + \phi_t + \frac{\delta}{2}\left(|\nabla\phi|^2 + \frac{1}{\mu^2}(\phi_z)^2\right) = 0, \qquad z = \delta\eta \tag{A.7}$$

$$\eta_t + \delta\nabla\eta \cdot \nabla\phi - \frac{1}{\mu^2}\phi_z = 0, \qquad z = \delta\eta \tag{A.8}$$

To develop an equation expressing volume flux conservation, we integrate (A.5) over z from $-h$ to $\delta\eta$. This gives

$$\int_{-h}^{\delta\eta} \phi_{zz}\, dz + \mu^2\nabla \cdot \int_{-h}^{\delta\eta} \nabla\phi\, dz - \delta\mu^2\nabla\phi\Big|_{z=\delta\eta} \cdot \nabla\eta - \mu^2\nabla\phi\Big|_{z=-h} \cdot \nabla h = 0 \tag{A.9}$$

Applying (A.6) and (A.7) in (A.9), we get

$$\eta_t + \nabla \cdot \int_{-h}^{\delta\eta} \nabla\phi\, dz = 0$$

or

$$\eta_t + \nabla \cdot M = 0, \quad M = \int_{-h}^{\delta\eta} \nabla\phi\, dz \tag{A.10}$$

Since ϕ is analytic, we may expand it as a power series in the vertical coordinate about $z = -h$

$$\phi(x, y, z, t) = \sum_{n=0}^{\infty} (z+h)^n \phi_n \tag{A.11}$$

where $\phi_n = \phi_n(x, y, t), \quad n = 1, 2, 3, \ldots$, whose order of magnitude is yet unknown. Following Mei (1989), we first evaluate the derivatives

$$\nabla\phi = \sum_{n=0}^{\infty} (z+h)^n \nabla\phi_n + \sum_{n=0}^{\infty} n(z+h)^{n-1} \phi_n \nabla h \tag{A.12}$$

$$\begin{aligned}
\nabla^2\phi =& \sum_{n=0}^{\infty} (z+h)^n \nabla^2\phi_n + \sum_{n=0}^{\infty} n(z+h)^{n-1} \nabla h \cdot \nabla\phi_n \\
&+ \sum_{n=0}^{\infty} n(z+h)^{n-1} \nabla \cdot (\phi_n \nabla h) + \sum_{n=0}^{\infty} n(n-1)(z+h)^{n-2} \phi_n \nabla h \cdot \nabla h \\
=& \sum_{n=0}^{\infty} (z+h)^n \nabla^2\phi_n + \sum_{n=0}^{\infty} (n+1)(z+h)^n \nabla h \cdot \nabla\phi_{n+1} \\
&+ \sum_{n=0}^{\infty} (n+1)(z+h)^n \nabla \cdot (\phi_{n+1} \nabla h) \\
&+ \sum_{n=0}^{\infty} (n+1)(n+2)(z+h)^n \phi_{n+2} \nabla h \cdot \nabla h
\end{aligned} \tag{A.13}$$

$$\phi_z = \sum_{n=0}^{\infty} n(z+h)^{n-1} \phi_n = \sum_{n=0}^{\infty} (n+1)(z+h)^n \phi_{n+1} \tag{A.14}$$

$$\phi_{zz} = \sum_{n=0}^{\infty} n(n+1)(z+h)^{n-1} \phi_{n+1} = \sum_{n=0}^{\infty} (n+1)(n+2)(z+h)^n \phi_{n+2} \tag{A.15}$$

Substituting (A.13) and (A.15) into (A.5), we obtain

$$\begin{aligned}
\phi_{zz} + \mu^2\nabla^2\phi = \sum_{n=0}^{\infty} (z+h)^n \Big[& (n+1)(n+2)\phi_{n+2} + \mu^2\nabla^2\phi_n \\
& + \mu^2(n+1)\nabla h \cdot \nabla\phi_{n+1} \\
& + \mu^2(n+1)\nabla \cdot (\phi_{n+1}\nabla h) \\
& + \mu^2(n+1)(n+2)\phi_{n+2}\nabla h \cdot \nabla h \Big] = 0
\end{aligned} \tag{A.16}$$

From (A.16), we have

$$\begin{aligned}(n+1)(n+2)\phi_{n+2} + \mu^2\nabla^2\phi_n = &-\mu^2(n+1)\nabla h\cdot\nabla\phi_{n+1}\\ &-\mu^2(n+1)\nabla\cdot(\phi_{n+1}\nabla h)\\ &-\mu^2(n+1)(n+2)\phi_{n+2}\nabla h\cdot\nabla h \end{aligned} \tag{A.17}$$

In the case of shallow water and slow variation of the bottom profile, i.e.

$$h, h', h'', etc. = O(\mu) \quad \text{where} \quad \mu \ll 1,$$

terms on the right-hand side of (A.17) can be ignored. This yields a recursive relation

$$\phi_{n+2} = \frac{-\mu^2\nabla^2\phi_n}{(n+1)(n+2)}, \quad n = 1, 2, 3, \ldots \tag{A.18}$$

On the horizontal bottom (A.6), we have

$$\phi_1 \equiv \phi_z = -\mu^2\nabla h\cdot\nabla\phi_0 \tag{A.19}$$

From (A.18) and (A.19), we can find

$$\begin{aligned}\phi_2 &= \frac{-\mu^2\nabla^2\phi_0}{2} = \frac{-\mu^2\nabla^2\phi_0}{2!}\\ \phi_3 &= \frac{\mu^4\nabla^2\phi_1}{2\cdot 3} = \frac{\mu^4\nabla^2(\nabla h\cdot\nabla\phi_0)}{3!}\\ &\vdots\end{aligned} \tag{A.20}$$

Substituting (A.19) and (A.20) into (A.11), we obtain

$$\phi(x,y,z,t) = \phi_0 - \mu^2(z+h)\nabla h\cdot\nabla\phi_0 - \mu^2\frac{(z+h)^2}{2}\nabla^2\phi_0 + O(\mu^4) \tag{A.21}$$

where ϕ_0 is the value of the velocity potential at $z = -h$. Following Nwogu (1993), we denote ϕ_α as the value of ϕ at $z = z_\alpha(x, y)$, or

$$\phi_\alpha = \phi_0 - \mu^2(h+z_\alpha)\nabla h\cdot\nabla\phi_0 - \mu^2\frac{(h+z_\alpha)^2}{2}\nabla^2\phi - 0 + O(\mu^4) \tag{A.22}$$

From (A.22), we get

$$\nabla\phi_\alpha = \nabla\phi_0 + O(\mu^2) \tag{A.23}$$

(A.21)-(A.22), we obtain

$$\phi = \phi_\alpha + \mu^2(z_\alpha - z)\nabla\cdot(h\nabla\phi_\alpha) + \frac{1}{2}\mu^2(z_\alpha^2 - z^2)\nabla^2\phi_\alpha + O(\mu^4) \tag{A.24}$$

where (A.23) is used. Substituting (A.24) into (A.9) and integrating

$$\eta_t + \nabla\cdot\left\{\int_{-h}^{\delta\eta}\nabla\phi_\alpha\,dz + \mu^2\int_{-h}^{\delta\eta}\nabla\Big[(z_\alpha - z)\nabla\cdot(h\nabla\phi_\alpha)\Big]\,dz + \frac{1}{2}\mu^2\int_{-h}^{\delta\eta}\nabla\left[(z_\alpha^2 - z^2)\nabla^2\phi_\alpha\right]\,dz\right\} + O(\mu^4) = 0 \tag{A.25}$$

or

$$\begin{aligned}\eta_t + \nabla\cdot\Bigg\{&(\delta\eta + h)\nabla\phi_\alpha + \mu^2(\delta\eta + h)z_\alpha\nabla(\nabla\cdot(h\nabla\phi_\alpha))\\ &+ \mu^2(\delta\eta + h)\nabla z_\alpha\nabla\cdot(h\nabla\phi_\alpha) - \mu^2\left(\frac{(\delta\eta)^2}{2} - \frac{h^2}{2}\right)\nabla(\nabla\cdot(h\nabla\phi_\alpha))\\ &+ \frac{1}{2}\mu^2(\delta\eta + h)z_\alpha^2\nabla(\nabla^2\phi_\alpha) + \mu^2(\delta\eta + h)z_\alpha\nabla z_\alpha\nabla^2\phi_\alpha\\ &- \frac{1}{2}\mu^2\left(\frac{(\delta\eta)^3}{3} - \frac{h^3}{3}\right)\nabla(\nabla^2\phi_\alpha)\Bigg\} + O(\mu^4) = 0\end{aligned} \tag{A.26}$$

or

$$\begin{aligned}\eta_t + \nabla\cdot\Bigg\{(h + \delta\eta)\Bigg[\nabla\phi_\alpha + \mu^2\Bigg\{\nabla\Big[z_\alpha\nabla\cdot(h\nabla\phi_\alpha) + \frac{z_\alpha^2}{2}\nabla^2\phi_\alpha\Big]\\ + (\frac{(h - \delta\eta)}{2})\nabla(\nabla\cdot(h\nabla\phi_\alpha))\\ - \frac{1}{6}(h^2 - \delta\eta h + (\delta\eta)^2)\nabla(\nabla^2\phi_\alpha)\Bigg]\Bigg\} + O(\mu^4) = 0\end{aligned} \tag{A.27}$$

Substituting (A.24) into Bernoulli equation (A.7), we get

$$\begin{aligned}
&\eta + \frac{\partial}{\partial t}\left[\phi_\alpha + \mu^2(z_\alpha - z)\nabla\cdot(h\nabla\phi_\alpha) + \frac{1}{2}\mu^2(z_\alpha^2 - z^2)\nabla^2\phi_\alpha\right] \\
&+ \frac{\delta}{2}\Bigg\{\left(\nabla\phi_\alpha + \mu^2\nabla\Big[(z_\alpha - z)\nabla\cdot(h\nabla\phi_\alpha)\Big] + \frac{1}{2}\mu^2\nabla\Big[(z_\alpha^2 - z^2)\nabla^2\phi_\alpha\Big]\right)^2 \\
&+ \frac{1}{\mu^2}\left(\frac{\partial}{\partial z}\Big[\phi_\alpha + \mu^2(z_\alpha - z)\nabla\cdot(h\nabla\phi_\alpha) + \frac{1}{2}\mu^2(z_\alpha^2 - z^2)\nabla^2\phi_\alpha\Big]\right)^2\Bigg\} \\
&+ O(\mu^4) = 0
\end{aligned} \tag{A.28}$$

or

$$\begin{aligned}
&\eta + \phi_{\alpha t} + \mu^2(z_\alpha - z)\nabla\cdot(h\nabla\phi_{\alpha t}) + \frac{1}{2}\mu^2(z_\alpha^2 - z^2)\nabla^2\phi_{\alpha t} \\
&+ \frac{\delta}{2}\Bigg[\Bigg(\nabla\phi_\alpha + \mu^2(z_\alpha - z)\nabla(\nabla\cdot(h\nabla\phi_\alpha)) + \mu^2\nabla z_\alpha(\nabla\cdot(h\nabla\phi_\alpha)) \\
&+ \frac{1}{2}\mu^2(z_\alpha^2 - z^2)\nabla(\nabla^2\phi_\alpha) + \mu^2 z_\alpha\nabla z_\alpha\nabla^2\phi_\alpha\Bigg)^2\Bigg] \\
&+ \frac{\delta}{2\mu^2}\Bigg[\Big(-\mu^2\nabla\cdot(h\nabla\phi_\alpha) - \mu^2 z\nabla^2\phi_\alpha\Big)^2\Bigg] + O(\mu^4) = 0
\end{aligned} \tag{A.29}$$

Let $z = \delta\eta$, we get

$$\begin{aligned}
&\eta + \phi_{\alpha t} + \mu^2\left[(z_\alpha - \delta\eta)\nabla\cdot(h\nabla\phi_{\alpha t}) + \frac{1}{2}(z_\alpha^2 - (\delta\eta)^2)\nabla^2\phi_{\alpha t}\right] \\
&+ \frac{\delta}{2}\Bigg[\nabla\phi_\alpha\cdot\nabla\phi_\alpha + 2\mu^2(z_\alpha - \delta\eta)\nabla\phi_\alpha\cdot\nabla(\nabla\cdot(h\nabla\phi_\alpha)) \\
&+ 2\mu^2\nabla\phi_\alpha\cdot\nabla z_\alpha\nabla\cdot(h\nabla\phi_\alpha) + \mu^2(z_\alpha^2 - (\delta\eta)^2)\nabla\phi_\alpha\cdot\nabla(\nabla^2\phi_\alpha) \\
&+ 2\mu^2 z_\alpha\nabla\phi_\alpha\cdot\nabla z_\alpha\nabla^2\phi_\alpha\Bigg] + \frac{\delta}{2}\mu^2(\nabla\cdot(h\nabla\phi_\alpha))^2 \\
&+ \delta\mu^2\nabla\cdot(h\nabla\phi_\alpha)\delta\eta\nabla^2\phi_\alpha + \frac{\delta}{2}\mu^2(\nabla\eta)^2(\nabla^2\phi_\alpha)^2 + O(\mu^4) = 0
\end{aligned} \tag{A.30}$$

or

$$\eta + \phi_{\alpha t} + \frac{\delta}{2}\nabla\phi_\alpha \cdot \nabla\phi_\alpha + \mu^2\left[(z_\alpha - \delta\eta)\nabla\cdot(h\nabla\phi_{\alpha t}) + \frac{1}{2}(z_\alpha^2 - (\delta\eta)^2)\nabla^2\phi_{\alpha t}\right]$$
$$+ \delta\mu^2\left\{\nabla\phi_\alpha \cdot \left[\nabla z_\alpha(\nabla\cdot(h\nabla\phi_\alpha)) + (z_\alpha - \delta\eta)\nabla(\nabla\cdot(h\nabla\phi_\alpha))\right]\right\}$$
$$+ \delta\mu^2\left\{\nabla\phi_\alpha \cdot \left[z_\alpha\nabla z_\alpha\nabla^2\phi_\alpha + \frac{1}{2}(z_\alpha^2 - (\delta\eta)^2)\nabla(\nabla^2\phi_\alpha)\right]\right\}$$
$$+ \delta\mu^2\left\{\frac{1}{2}(\nabla\cdot(h\nabla\phi_\alpha))^2 + \delta\eta\nabla\cdot(h\nabla\phi_\alpha)\nabla^2\phi_\alpha + \frac{1}{2}(\delta\eta)^2(\nabla^2\phi_\alpha)^2\right\}$$
$$+ O(\mu^4) = 0 \tag{A.31}$$

Differentiating on the both side of (A.31), we obtain

$$\nabla\eta + \nabla\phi_{\alpha t} + \frac{\delta}{2}\nabla\phi_\alpha \cdot \nabla\phi_\alpha + \mu^2\nabla\left[(z_\alpha - \delta\eta)\nabla\cdot(h\nabla\phi_{\alpha t}) + \frac{1}{2}(z_\alpha^2 - (\delta\eta)^2)\nabla^2\phi_{\alpha t}\right]$$
$$+ \delta\mu^2\nabla\left\{\nabla\phi_\alpha \cdot \left[\nabla z_\alpha(\nabla\cdot(h\nabla\phi_\alpha)) + (z_\alpha - \delta\eta)\nabla(\nabla\cdot(h\nabla\phi_\alpha))\right]\right\}$$
$$+ \delta\mu^2\nabla\left\{\nabla\phi_\alpha \cdot \left[z_\alpha\nabla z_\alpha\nabla^2\phi_\alpha + \frac{1}{2}(z_\alpha^2 - (\delta\eta)^2)\nabla(\nabla^2\phi_\alpha)\right]\right\}$$
$$+ \delta\mu^2\nabla\left\{\frac{1}{2}(\nabla\cdot(h\nabla\phi_\alpha))^2 + \delta\eta\nabla\cdot(h\nabla\phi_\alpha)\nabla^2\phi_\alpha + \frac{1}{2}(\delta\eta)^2(\nabla^2\phi_\alpha)^2\right\}$$
$$+ O(\mu^4) = 0 \tag{A.32}$$

Differentiating (A.24) on the both side, we get

$$\nabla\phi(x, y, z, t) = \nabla\phi_\alpha(x, y, t) + O(\mu^2) \tag{A.33}$$

Substituting (A.33) into (A.24), we obtain

$$\phi = \phi_\alpha + \mu^2(z_\alpha - z)\nabla\cdot(h\nabla\phi) + \frac{1}{2}\mu^2(z_\alpha^2 - z^2)\nabla^2\phi + O(\mu^4) \tag{A.34}$$

Differentiating (A.34) on the both side and evaluating at $z = z_\alpha$, we get

$$\nabla\phi\Big|_{z=z_\alpha} = \nabla\phi_\alpha + \mu^2\nabla z_\alpha\nabla\cdot(h\nabla\phi\Big|_{z=z_\alpha}) + \mu^2 z_\alpha\nabla z_\alpha\nabla^2\phi\Big|_{z=z_\alpha} + O(\mu^4) \tag{A.35}$$

Since $\nabla\phi\Big|_{z=z_\alpha} = \mathbf{u}_\alpha$, (A.35) of the form

$$\nabla\phi_\alpha = \mathbf{u}_\alpha - \mu^2\nabla z_\alpha\nabla\cdot(h\mathbf{u}_\alpha) - \mu^2 z_\alpha\nabla z_\alpha\nabla\cdot\mathbf{u}_\alpha + O(\mu^4) \tag{A.36}$$

Substituting (A.36) into (A.27) and (A.33) and retaining terms to $O(\mu^2)$ up to all orders in δ, we obtain a fully nonlinear version of the model with conservation equation

$$\begin{aligned}\eta_t + \nabla\cdot\Bigg\{(h+\delta\eta)\Bigg[\mathbf{u}_\alpha + \mu^2\Bigg\{\nabla\Big[z_\alpha + \frac{(h-\delta\eta)}{2}\Big]\nabla(\nabla\cdot(h\nabla\mathbf{u}_\alpha)) \\ + \Big[\frac{z_\alpha^2}{2} - \frac{1}{6}(h^2 - \delta\eta h + (\delta\eta)^2)\Big]\nabla(\nabla\cdot\mathbf{u}_\alpha)\Bigg\}\Bigg]\Bigg\} + O(\mu^4) = 0\end{aligned} \tag{A.37}$$

and momentum equation

$$\begin{aligned}&\mathbf{u}_{\alpha t} + \frac{\delta}{2}\nabla(\mathbf{u}_\alpha\cdot\mathbf{u}_\alpha) + \nabla\eta + \mu^2\Bigg\{\frac{1}{2}z_\alpha^2\nabla(\nabla\cdot\mathbf{u}_{\alpha t}) + z_\alpha\nabla(\nabla\cdot(h\mathbf{u}_{\alpha t})) \\ &+ \nabla\left[\frac{1}{2}(\delta\eta)^2\nabla\cdot\mathbf{u}_{\alpha t} + \delta\eta\nabla\cdot(h\mathbf{u}_{\alpha t})\right]\Bigg\} \\ &+ \delta\mu^2\Bigg\{\nabla\left[(z_\alpha - \delta\eta)(\mathbf{u}_\alpha\cdot\nabla)(\nabla\cdot(h\mathbf{u}_\alpha)) + \frac{1}{2}(z_\alpha^2 - (\delta\eta)^2)(\mathbf{u}_\alpha\cdot\nabla)(\nabla\cdot\mathbf{u}_\alpha)\right] \\ &+ \frac{1}{2}\nabla\left[\Big(\nabla\cdot(h\mathbf{u}_\alpha) + \delta\eta\nabla\cdot\mathbf{u}_\alpha\Big)^2\right]\Bigg\} + O(\mu^4) = 0\end{aligned} \tag{A.38}$$

or

$$\mathbf{u}_{\alpha t} + \delta(\nabla\cdot\mathbf{u}_\alpha)\mathbf{u}_\alpha + \nabla\eta + \mu^2\mathbf{V_1} + \delta\mu^2\mathbf{V_1} + O(\mu^4) = 0 \tag{A.39}$$

where

$$\frac{\delta}{2}\nabla(\mathbf{u}_\alpha\cdot\mathbf{u}_\alpha) = \delta(\nabla\cdot\mathbf{u}_\alpha)\mathbf{u}_\alpha, \tag{A.40}$$

$$\mathbf{V_1} = \frac{1}{2}z_\alpha^2\nabla(\nabla\cdot\mathbf{u}_{\alpha t}) + z_\alpha\nabla(\nabla\cdot(h\mathbf{u}_{\alpha t})) + \nabla\left[\frac{1}{2}(\delta\eta)^2\nabla\cdot\mathbf{u}_{\alpha t} + \delta\eta\nabla\cdot(h\mathbf{u}_{\alpha t})\right] \tag{A.41}$$

and

$$\begin{aligned}\mathbf{V_2} =&\nabla\left[(z_\alpha - \delta\eta)(\mathbf{u}_\alpha\cdot\nabla)(\nabla\cdot(h\mathbf{u}_\alpha)) + \frac{1}{2}(z_\alpha^2 - (\delta\eta)^2)(\mathbf{u}_\alpha\cdot\nabla)(\nabla\cdot\mathbf{u}_\alpha)\right] \\ &+ \frac{1}{2}\nabla\left[\Big(\nabla\cdot(h\mathbf{u}_\alpha) + \delta\eta\nabla\cdot\mathbf{u}_\alpha\Big)^2\right]\end{aligned} \tag{A.42}$$

Appendix II

Bottom friction, Wave Breaking, Moving Shorelines, and Subgrid Turbulence

In this study, the Boussinesq model are modified with extensions to cover bottom friction, Wave Breaking, Moving Shorelines, and Subgrid Turbulence effects developed by Chen *et al.* (2000) and Kennedy *et al.* (2000). The bottom friction given by

$$(F_b, G_b) = \frac{K}{h+\eta}\mathbf{u}_\alpha \left|\mathbf{u}_\alpha\right| \tag{B.1}$$

where $K = 1 \times 10^{-5}$ is the friction coefficient.

For wave breaking in shallow water based on Kennedy *et al.* (2000) defined by

$$F_{br} = \frac{1}{h+\eta}\Big[(\nu((h+\eta)u_\alpha)_x)_x + \frac{1}{2}(\nu(((h+\eta)u_\alpha)_y + ((h+\eta)v_\alpha)_x))_y\Big] \tag{B.2}$$

$$G_{br} = \frac{1}{h+\eta}\Big[\frac{1}{2}(\nu(((h+\eta)v_\alpha)_x + ((h+\eta)u_\alpha)_y))_x + (\nu((h+\eta)v_\alpha)_y)_y\Big] \tag{B.3}$$

where superscripts x and y represent the directions in the horizontal plane, subscripts x and y denote spatial derivatives, and ν is the eddy viscosity localized on the front face of the breaking wave, which define as

$$\nu = B\delta^2|(h+\eta)\nabla \cdot \mathbf{M}| \tag{B.4}$$

where δ is a mixing length coefficient with an empirical value of $\delta = 1.2$. The quantity

B that controls the occurrence of energy dissipation is given by

$$B = \begin{cases} 1, & \eta_t \geq 2\eta_t^* \\ \frac{\eta_t}{\eta_t^*} - 1, & \eta_t^* < \eta_t \leq 2\eta_t^* \\ 0, & \eta_t \leq \eta_t^* \end{cases} \tag{B.5}$$

and the onset and cessation of wave breaking using the parameter, η_t^*, which is defined as

$$\eta_t^* = \begin{cases} \eta_t^{(F)}, & t \geq T^* \\ \eta_t^{(I)} + \frac{t-t_0}{T^*}\left(\eta_t^{(F)} - \eta_t^{(I)}\right), & 0 \leq t - t_0 < T^* \end{cases} \tag{B.6}$$

where T^* is the transition time, t_0 is the time when the wave breaking occurs, and $t - t_0$ is the age of the breaking event. The value of $\eta_t^{(I)}$ varies between $0.35\sqrt{gh}$ and $0.65\sqrt{gh}$, while the values of $\eta_t^{(F)}$, and T^* are $0.15\sqrt{gh}$, and $5\sqrt{h/g}$, respectively. The construction and verification of the breaking model was detail by Kennedy *et al.* (2000).

The factors Λ and κ in (3.10) were introduced by Kennedy *et al.* (2000) and Chen *et al.* (2000) to implement a porous (i.e., absorbing) beach method, used to keep the subaerial portion of the model grid computationally active and to simplify the calculation of runup on dry shorelines. These are given by

$$\kappa = \begin{cases} \delta + (1-\delta)\mathrm{e}^{\lambda(\frac{\eta - z^*}{h_0})}, & \eta \leq z^* \\ 1, & \eta > z^* \end{cases} \tag{B.7}$$

and

$$\Lambda = \begin{cases} \delta(\eta + h_0) + \frac{(1-\delta)h_0}{\lambda}\left(e^{\lambda\frac{(\eta - z^*)}{h_0}} - e^{-\lambda\frac{(h_0 + z^*)}{h_0}}\right), & \eta \leq z^* \\ (\eta - z^*) + \delta(z^* + h_0) + \frac{(1-\delta)h_0}{\lambda}\left(1 - e^{-\lambda\frac{(h_0 + z^*)}{h_0}}\right), & \eta > z^* \end{cases} \tag{B.8}$$

h_0 represents the porous beach depth, which must be deeper than the depth of maximum wave rundown during a calculation. The choice of z^* is discussed by *Kennedy et al.* (2000) given by

$$z^* = \frac{z^s}{1-\delta} + h_0\Big(\frac{\delta}{1-\delta} + \frac{1}{\lambda}\Big) \tag{B.9}$$

where z^s is the elevation of the solid seabed. Here $\delta = 0.08$ and $\lambda = 25$, based on studies of a number of tsunami runup events [*Watts et al.*, 2003; *Day et al.*, 2005].

The Smagorinsky type subgrid model (Smagorinsky 1963) to account for the effect of the resultant eddy viscosity on the underlying flow.

$$F_{bs} = \frac{1}{h+\eta}\Big[(\nu_s((h+\eta)u_\alpha)_x)_x + \frac{1}{2}(\nu_s(((h+\eta)u_\alpha)_y + ((h+\eta)v_\alpha)_x))_y\Big] \tag{B.10}$$

$$G_{bs} = \frac{1}{h+\eta}\Big[\frac{1}{2}(\nu_s(((h+\eta)v_\alpha)_x + ((h+\eta)u_\alpha)_y))_x + (\nu_s((h+\eta)v_\alpha)_y)_y\Big] \tag{B.11}$$

where ν_s is the eddy viscosity due to the subgrid turbulence.

$$\nu_s = c_m \Delta x \Delta y\Big[(U_x)^2 + (V_y)^2 + \frac{1}{2}(U_y + V_x)^2\Big]^{\frac{1}{2}} \tag{B.12}$$

in which U and V are the velocity components of the time averaged underlying current field, Δx and Δy are the grid spacing in the x and y directions, respectively, and c_m is the mixing coefficient with the default value of 0.2. In the course of simulation, the underlying current field obtained by averaging the instantaneous velocity over two peak wave periods and update ν_α accordingly.

Appendix III

Numerical scheme

C.1 Finite difference Scheme

Numerical solutions of Boussinesq equations can be significantly corrupted if truncation errors, arising from differencing of the leading order wave equation terms, are allowed to grow in size and become comparable to the terms describing the weak dispersion effects.

Following Wei *et al.* (1995) and Kirby *et al.* (1998), a composite fourth-order Adams Bashforth-Mounlton scheme (utilizing a third-order Adams-Bashforth predictor step and forth-order Adams-Moulton corrector step) is used to step the model forward in time. Terms involving first-order spatial derivatives are differenced to $O(\Delta x^4)$ acuracy by utilizing a five-point formula. All errors involved in solving the underlying nonlinear shallow water equations are thus reduced to 4th order in grid spacing and time step size. Spatial and temporal differencing of the higher-order dispersion terms is done to second-order accuracy, which again reduces the truncation errors to a size smaller than those terms themselves. No further back-substitution of apparent truncation error terms is performed.

Time-differencing

The arrangement of cross-differentiated and nonlinear time derivative terms on the right hand side of equations (3.6)-(3.7) marks the resulting set of left-hand sides

purely tridiagonal. The governing equations are finite-different on a centered grid in $x = i\Delta x, y = j\Delta y, t = n\Delta t$. Level n refers to information at the present, known time level. The predictor step is the third-order explicit Adams-Bashforth scheme, given by

$$\eta_{i,j}^{n+1} = \eta_{i,j}^{n} + \frac{\Delta t}{12}[23(E')_{i,j}^{n} - 16(E')_{i,j}^{n-1} + 5(E')_{i,j}^{n-2}] \tag{C.1}$$

$$\begin{aligned} U_{i,j}^{n+1} = U_{i,j}^{n} &+ \frac{\Delta t}{12}[23(F')_{i,j}^{n} - 16(F')_{i,j}^{n-1} + 5(F')_{i,j}^{n-2}] \\ &+ \frac{\nabla t}{12}[23((F_1)_t)_{i,j}^{n} - 16((F_1)_t)_{i,j}^{n-1} + 5((F_1)_t)_{i,j}^{n-2}] \end{aligned} \tag{C.2}$$

$$\begin{aligned} V_{i,j}^{n+1} = V_{i,j}^{n} &+ \frac{\Delta t}{12}[23(G')_{i,j}^{n} - 16(G')_{i,j}^{n-1} + 5(G')_{i,j}^{n-2}] \\ &+ \frac{\nabla t}{12}[23((G_1)_t)_{i,j}^{n} - 16((G_1)_t)_{i,j}^{n-1} + 5((G_1)_t)_{i,j}^{n-2}] \end{aligned} \tag{C.3}$$

where

$$E' = E + \gamma E_2 \tag{C.4}$$

$$F' = F + \gamma(F_2 + F^t) + F_{br} + F_b + F_{sp} \tag{C.5}$$

$$G' = G + \gamma(G_2 + G^t) + G_{br} + G_b + G_{sp} \tag{C.6}$$

All information on the right hand sides of (C.1)-(C.3) is known from previous calculations. The values of $\eta_{i,j}^{n+1}$ are thus straightforward to obtain. The elevation of horizontal velocities at the new time level, however, requires simultaneous solution of tridiagonal matrix systems which are linear in the unkhowns at level $n+1$. Specifically, for a given j, $u_{i,j}^{n+1}(i = 1, 2, ..., M)$ are obtained through tridiagonal matrix solution. Similarly, $v_{i,j}^{n+1}(j = 1, 2, ..., N)$ are solved by a system of tridiagonal matrix equation for given i. The matrices involved are constant in time and may be pre-factored, inverted and stored for use at each time step.

After the predicted values of $\{\eta, u, v\}_{i,j}^{n+1}$ are evaluated, we obtain the corresponding quantities of $\{E', F', G'\}_{i,j}$ at time levels $(n+1), (n), (n-1), (n-2)$, and apply the

fourth-order Adams-Moulton corrector method

$$\eta_{i,j}^{n+1} = \eta_{i,j}^{n} + \frac{\Delta t}{24}[9(E')_{i,j}^{n+1} + 19(E')_{i,j}^{n} - 5(E')_{i,j}^{n-1} + (E')_{i,j}^{n-2}] \tag{C.7}$$

$$\begin{aligned} U_{i,j}^{n+1} = U_{i,j}^{n} &+ \frac{\Delta t}{24}[9(F')_{i,j}^{n+1} + 19(F')_{i,j}^{n} - 5(F')_{i,j}^{n-1} + (F')_{i,j}^{n-2}] \\ &+ \frac{\nabla t}{24}[9((F_1)_t)_{i,j}^{n+1} + 19((F_1)_t)_{i,j}^{n} - 5((F_1)_t)_{i,j}^{n-1} + ((F_1)_t)_{i,j}^{n-2}] \end{aligned} \tag{C.8}$$

$$\begin{aligned} V_{i,j}^{n+1} = V_{i,j}^{n} &+ \frac{\Delta t}{24}[9(G')_{i,j}^{n+1} + 19(G')_{i,j}^{n} - 5(G')_{i,j}^{n-1} + (G')_{i,j}^{n-2}] \\ &+ \frac{\Delta t}{24}[9((G_1)_t)_{i,j}^{n+1} + 19((G_1)_t)_{i,j}^{n} - 5((G_1)_t)_{i,j}^{n-1} + ((G_1)_t)_{i,j}^{n-2}] \end{aligned} \tag{C.9}$$

From the definition, we see that calculation of F^t and G_t at certain time level requires the corresponding values of u_t and v_t. Also, the terms $(F_1)_t$ and $(G_1)_t$ involves time derivatives. Defining quantity w as

$$w = \{u, v, F_1, G_1\} \tag{C.10}$$

then its time derivatives for predictor stage are

$$(w_t)_{i,j}^{n} = \frac{1}{2\Delta t}[3w_{i,j}^{n} - 4w_{i,j}^{n-1} + w_{i,j}^{n-2}] + O(\Delta t^2) \tag{C.11}$$

$$(w_t)_{i,j}^{n-1} = \frac{1}{2\Delta t}[w_{i,j}^{n} - w_{i,j}^{n-2}] + O(\Delta t^2) \tag{C.12}$$

$$(w_t)_{i,j}^{n-2} = \frac{-1}{2\Delta t}[3w_{i,j}^{n-2} - 4w_{i,j}^{n-1} + w_{i,j}^{n}] + O(\Delta t^2) \tag{C.13}$$

For the corrector stage, we evaluate w_t according to

$$(w_t)_{i,j}^{n+1} = \frac{1}{6\Delta t}[11w_{i,j}^{n+1} - 18w_{i,j}^{n} + 9w_{i,j}^{n-1} - 2w_{i,j}^{n-2}] + O(\Delta t^3) \tag{C.14}$$

$$(w_t)_{i,j}^{n} = \frac{1}{6\Delta t}[2w_{i,j}^{n+1} + 3w_{i,j}^{n} - 6w_{i,j}^{n-1} + w_{i,j}^{n-2}] + O(\Delta t^3) \tag{C.15}$$

$$(w_t)_{i,j}^{n-1} = \frac{-1}{6\Delta t}[2w_{i,j}^{n-2} + 3w_{i,j}^{n-1} - 6w_{i,j}^{n} + w_{i,j}^{n+1}] + O(\Delta t^3) \tag{C.16}$$

$$(w_t)_{i,j}^{n-2} = \frac{-1}{6\Delta t}[11w_{i,j}^{n-2} - 18w_{i,j}^{n-1} + 9w_{i,j}^{n} - 2w_{i,j}^{n+1}] + O(\Delta t^3) \tag{C.17}$$

By substituting $(F_1)_t$ and $(G_1)_t$ into the equation(C.2),(C.3),(C.8)and (C.9), the last terms in these equations reduce to

$$\frac{\Delta t}{12}[23(w_t)^n_{i,j} - 16(w_t)^{n-1}_{i,j} + 5w_t{}^{n-2}_{i,j}] = 2w^n_{i,j} - 3w^{n-1}_{i,j} + w^{n-2}_{i,j} \tag{C.18}$$

$$\frac{\Delta t}{24}[9(w_t)^{n+1}_{i,j} + 19(w_t)^n_{i,j} - 5(w_t)^{n-1}_{i,j} + w_t{}^{n-2}_{i,j}] = w^{n+1}_{i,j} - w^n_{i,j} \tag{C.19}$$

where $w = \{F_1, G_1\}$ The corrector step is iterated until the error between two successive results reaches a required limit. The error is computed for each of the three dependent variables η, u and v and is defined as

$$\Delta f = \frac{\sum_{i=1,j=1}^{i=M,j=N} \left| f^{n+1}_{i,j} - f^*_{i,j} \right|}{\sum_{i=1,j=1}^{i=M,j=N} \left| f^{n+1}_{i,j} \right|} \tag{C.20}$$

where $f = \{\eta, u, v\}$, f^{n+1} and f^* denote the current and previous results, respectively. The corrector step is iterated if any of Δf's exceeds 10^{-4} or 10^{-3}. For "cold start"running of the model, the denominator in (C.20) is zero initially, which will result in infinite value of Δf. To eliminate this problem, we first compute the corresponding denominator. If value of the denominator is smaller than a small value (say, 10^{-3}), then only numerator from (C.20) is used for iteration errors.

For weakly nonlinear case, the scheme typically requires no iteration unless problems arise from boundaries, or inappropriate values for $\Delta x, \Delta y$ and Δt are used. For strong nonlinearity, however, the model tends to take more iterations. Further analysis shows that the iterated results oscillate around the desired solution. To increase the convergence rate, we apply an over-relaxation technique to the iteration stage. Writing the previous and current iterated values as $f^*_{i,j}$ and $f_{i,j}$, then the adjusted valued $f^r_{i,j}$ for over-relaxation is given by

$$f^r_{i,j} = (1 - R)f^*_{i,j} + Rf_{i,j} \tag{C.21}$$

where R is a coefficient which is in the range of (0,1). In all computations, it is found that $R = 0.2$ gives quite satisfactory results.

Spatial differencing

For first order spatial derivatives, the following five-point difference schemes are used

$$(w_x)_{1,j} = \frac{1}{12\Delta x}(-25w_{1,j} + 48w_{2,j} - 36w_{3,j} + 16w_{4,j} - 3w_{5,j}) \tag{C.22}$$

$$(w_x)_{2,j} = \frac{1}{12\Delta x}(-3w_{1,j} - 10w_{2,j} + 18w_{3,j} - 6w_{4,j} + w_{5,j}) \tag{C.23}$$

$$(w_x)_{i,j} = \frac{1}{12\Delta x}[8(w_{i+1,j} - w_{i-1,j}) - (w_{i+2,j} - w_{i-2,j})] \tag{C.24}$$

$$(i = 3, 4, ..., M-2)$$

$$(w_x)_{M-1,j} = \frac{1}{12\Delta x}(3w_{M,j} + 10w_{M_1,j} - 18w_{M_2,j} + 6w_{M_3,j} - w_{M_4,j}) \tag{C.25}$$

$$(w_x)_{M,j} = \frac{-1}{12\Delta x}(25w_{M,j} - 48w_{M_1,j} + 36w_{M_2,j} - 16w_{M_3,j} + 3w_{M_4,j}) \tag{C.26}$$

where $w = \{\eta, u, v\}$, $M_k = M - k(k = 1, 2, 3, 4)$, and M is the total number of grid point in x direction.

For second order derivatives, we use three-point difference schemes

$$(w_{xx})_{i,j} = \frac{w_{i+1,j} - 2w_{i,j} + w_{i-1,j}}{(\Delta x)^2} \tag{C.27}$$

$$(i = 2, 3, ..., M-1)$$

Similar expressions can be obtained for derivatives with respect to y. For mixed derivatives, we use

$$(w_{xy})_{i,j} = \frac{w_{i+1,j+1} + w_{i-1,j-1} - w_{i-1,j+1} - w_{i+1,j-1}}{4\Delta x \Delta y} \tag{C.28}$$

$$(i = 2, 3, ..., M-1; j = 2, 3, ..., N-1)$$

C.2 Boundary Conditions

Reflective Boundaries

For a perfectly reflecting vertical wall, the horizontal velocity normal to the wall is always zero, i.e.

$$\mathbf{u} \cdot \mathbf{n} = 0; \qquad (x, y) \in \partial\Omega \tag{C.29}$$

The corresponding values of surface elevation and tangential velocity, the normal derivatives as zero, i.e.

$$\frac{\partial \mathbf{u}}{\partial \mathbf{n}} = 0; \qquad (x, y) \in \partial\Omega \tag{C.30}$$

$$\frac{\partial \eta}{\partial \mathbf{n}} = 0; \qquad (x, y) \in \partial\Omega \tag{C.31}$$

where Ω = the fluid domain, $\partial\Omega$ = the boundary and (x, y) = a position in the domain.

Absorbing Boundaries

There are several types of absorbing boundary condition which allows waves to propagate out of domain with minimum reflection. A sponge layer boundary condition is used here since it is able to damp wave energy for a wide range of frequencies and directions. Although extra grid points are needs, it is justified to apply sponge layer due to the decreasing cost of computer storage and the stability of the numerical model.

To absorb wave energy, artificial damping terms F_{sp} and G_{sp} are added to the right hand side of the momentum equations (3.6) and (3.7), respectively. The damping terms are defined as

$$F_{sp} = -w_1(x, y)u + w_2(x, y)(u_{xx} + u_{yy}) + w_3(x, y)\sqrt{\frac{g}{h}}\eta \tag{C.32}$$

$$G_{sp} = -w_1(x, y)v + w_2(x, y)(v_{xx} + v_{yy}) + w_3(x, y)\sqrt{\frac{g}{h}}\eta \tag{C.33}$$

where w_1,w_2 and w_3 are functions for three different kinds of damping mechanism, which were referred to as Newtonian cooling, viscous damping, and sponge filter, respectively (Israeli and Orszag, 1981). Assuming that there is only one sponge layer on the right end of domain, $w_i, \quad i = 1,\ 2,\ 3$ defined as

$$w_i(x,y) = \begin{cases} c_i \omega f(x), & x_s < x < x_l \\ 0, & elsewhere \end{cases} \tag{C.34}$$

where $i = 1,\ 2,\ 3,\ c_i$ are constant coefficients corresponding to the three damping functions, ω is frequency of wave to be damped, x_s is starting coordinate of damping layer (the computing domain is from $x = 0$ to $x = x_l$) and $f(x)$ is a smooth monotonically increasing function varying from 0 to 1 when x varies from x_s to x_l. Function $f(x)$ is defined as

$$f(x) = \frac{e^{[(x-x_s)/(x_l-x_s)]^2-1}}{e-1}, \qquad x_s < x < x_l. \tag{C.35}$$

The width of the damping layer (*i.e.* $x_l - x_s$) is usually taken to be two or three wave lengths.

VITAE

Mr.Narongrit Kaewbangak was born in August 22, 1981, in Mahasarakham, Thailand. He received a bachelor degree in Mathematics from the Department of Mathematics, Faculty of Science, Khonkean University, Khonkean, Thailand in 2004.

PUBLICATION

- Asavanant, J., Ioualalen, M., Kaewbanjak, N., Grilli, S., Watts, P., Kirby, J. and Shi, F. "Numerical Simulation of the December 26, 2004: Indian Ocean Tsunami", *International Conference on High Performance Scientific Computing (HPSC Hanoi 2006)*, March 4-10, 2006.

- Kaewbanjak, N., Asavanant, J., Ioualalen, M., Grilli, S., Watts, P. and Kirby, J "Numerical Model for the December 26, 2004 Tsunami", *Annual National Symposium on Computational Science and Engineering (ANSCSE10)*, March 22-24, 2006.